

Immersed Boundary Double Layer method: An introduction of methodology on the Helmholtz equation

Brittany J. Leathers^a, Robert D. Guy^a

^a*Department of Mathematics, University of California, Davis, Davis, CA 95616-5270, USA*

Abstract

The Immersed Boundary (IB) method of Peskin (J. Comput. Phys., 1977) is useful for problems that involve fluid-structure interactions or complex geometries. By making use of a regular Cartesian grid that is independent of the geometry, the IB framework yields a robust numerical scheme that can efficiently handle immersed deformable structures. Additionally, the IB method has been adapted to problems with prescribed motion and other PDEs with given boundary data. IB methods for these problems traditionally involve penalty forces which only approximately satisfy boundary conditions, or they are formulated as constraint problems. In the latter approach, one must find the unknown forces by solving an equation that corresponds to a poorly conditioned first-kind integral equation. This operation can therefore require a large number of iterations of a Krylov method, and since a time-dependent problem requires this solve at each step in time, this method can be prohibitively inefficient without preconditioning. This work introduces a new, well-conditioned IB formulation for boundary value problems, called the Immersed Boundary Double Layer (IBDL) method. In order to lay the groundwork for similar formulations of Stokes and Navier-Stokes equations, this paper focuses on the Poisson and Helmholtz equations to introduce the methodology and to demonstrate its efficiency over the original constraint method. In this double layer formulation, the equation for the unknown boundary distribution corresponds to a well-conditioned second-kind integral equation that can be solved efficiently with a small number of iterations of a Krylov method without preconditioning. Furthermore, the iteration count is independent of both the mesh size and spacing of the immersed boundary points. The method converges away from the boundary, and when combined with a local interpolation, it converges in the entire PDE domain. Additionally, while the original constraint method applies only to Dirichlet problems, the IBDL formulation can also be used for Neumann boundary conditions.

Keywords: Immersed Boundary Method, Boundary Integral Equation, Double Layer Potential, Finite Difference, Cartesian Grid, Partial Differential Equation, Complex Geometry

1. Introduction

The Immersed Boundary (IB) method [1, 2] is a valuable numerical tool for fluid-structure interactions. It was initially developed by Peskin for problems involving elastic, deformable structures, such as those involved in cardiac dynamics [3, 4, 5, 6, 7]. However, the robustness and simplicity of the IB method has led to its use in many different applications (see [8, 9, 10], for just a few). Additionally, since its creation, there have been many developments and variations in the IB method. For instance, the IB framework has been altered to incorporate porous boundaries [11, 12] and model elastic rods with a curvature or twist [13, 14]. It has also been adapted to the flow of non-Newtonian fluids [15, 16] and coupled with internal force mechanisms to model swimming organisms [17, 18]. In recent years, work has been done to apply the Immersed Boundary framework to problems involving prescribed boundary values [19, 20, 21, 22, 23, 24], which is the category of problems that this paper addresses.

The robustness of the IB method comes from its use of two coordinate systems: a Lagrangian system that moves with the structure and a fixed Eulerian system on which the fluid equations are solved. It uses convolutions with discrete delta functions to link these systems together and map forces from the structure to the grid. One can then solve the PDE on a regular Cartesian mesh. This elimination of the physical boundary makes it possible to use a PDE solver that is efficient and independent of the geometry of the structure.

As stated, this paper will focus on problems involving prescribed boundary values. In the field of fluid dynamics, this includes the motion of rigid bodies and fluid flow through a domain with stationary boundaries or boundaries with prescribed motion. Since the IB method bypasses the need for a conforming mesh, it also has obvious advantages in the broader case of solving PDEs on complex domains. In this paper, we focus on scalar elliptic boundary value problems to introduce a new IB method.

When the IB method is applied to deformable structures, the boundary force density is found using a constitutive law from the structure characteristics [2], but in the case of rigid bodies, one needs a different way to find or interpret the boundary force. There have been several routes taken to use the IB framework in these situations. One method is to consider the Lagrangian points to be tethered to specified locations by springs. The boundary force is then interpreted as the spring restoring force, penalizing deviations from the prescribed boundary position [25, 26, 27, 28]. By using the IB framework, such penalty methods can be efficiently implemented, but they use parameters, such as spring constants, to approximate a rigid limit, and the required magnitude of the appropriate parameter leads to numerically stiff equations that necessitate very small timesteps.

Another approach for applying the IB method to a rigid body problem consists of viewing the boundary force density as a Lagrange multiplier, used to

enforce the no-slip boundary condition [19]. Section 2.1 gives a description of such a method as applied to a scalar PDE. In this IB constraint method, the velocity and force are both unknowns in an algebraic system. One way to solve this system is to invert the Schur complement to solve first for the Lagrange multiplier force and then for the velocity. The main disadvantage of such a method is that this operator suffers from poor conditioning [20]. Furthermore, the conditioning of the discrete problem worsens when the Cartesian grid is refined or when the Lagrangian point spacing is refined relative to the grid. To avoid solving the fully discretized constraint problem, most numerical methods using this constraint approach rely on some form of time step splitting [19, 21, 22, 23, 24]. Taira and Colonius [19], for example, solve a simpler unconstrained system for an intermediate velocity, use this velocity to find pressure and the unknown boundary force, and then complete a projection step to remove non-divergence-free and slip components of the velocity. However, like the penalty methods, these fractional step methods only satisfy the constraint equations *approximately*, which can result in fluid penetration into a rigid body. Additionally, such a method cannot be used for steady Stokes or other time-independent PDE.

However, if instead of a time-splitting scheme, one inverts the Schur complement with a Krylov method, the number of iterations required could be very large due to its poor conditioning. The computational cost then becomes prohibitive for a time-dependent problem, when this solve would be required at each time step. One way around this is to design a preconditioner [29, 30, 31], such as the physics-based approximation of the Schur complement constructed by Kallemov et al. [20]. A preconditioner can allow for a more efficient solution to the constraint problem, but developing and implementing one is a nontrivial undertaking, and such a preconditioner can involve computing the inverse of a dense matrix, which can be computationally expensive when the number of boundary points is large. Another limitation is that in order to control the conditioning, there is often a requirement that the boundary points be spaced to about twice the grid spacing, which, depending on the application and the Eulerian-Lagrangian coupling scheme, may result in decreased accuracy of the solution [20, 32, 33].

In this paper, we present a reformulated Immersed Boundary method for prescribed boundary values. In order to lay the groundwork for similar formulations of Stokes and Navier-Stokes equations, in this paper, we focus on the Poisson and Helmholtz equations to introduce the methodology. Like the IB constraint method, our method enforces the boundary conditions *exactly*, but the resulting linear system is very well-conditioned. We can therefore solve it with an unpreconditioned Krylov method with very few iterations. This conditioning does not worsen as we refine the mesh, nor as we tighten the spacing of our boundary points relative to the grid. We are therefore able to avoid the need for a preconditioner altogether.

We formulate this new IB method by utilizing a connection between the IB constraint method and a single layer boundary integral equation. Bound-

ary integral methods rely on reformulating a boundary value problem as an integral equation with an unknown density on the boundary. These methods are particularly useful for linear, elliptic, and homogeneous PDE [34]. One advantage of these methods, which we exploit, is that there are well-conditioned integral representations available. For example, for the Helmholtz equation or Stokes equations, we can derive single and double layer integral representations. When combined with Dirichlet boundary conditions, a double layer representation results in a second-kind integral equation. In this case, the operator we need to invert is well-conditioned. Therefore, these double layer representations have been frequently utilized within boundary integral methods [35, 36, 37, 38].

There are, however, some disadvantages to directly using boundary integral equations. Firstly, for a typical boundary integral method, once the boundary density is found, it is expensive to evaluate the solution on an entire grid, whereas by using efficient solvers, the IB method can do this quickly. Additionally, in order to directly implement integral methods, one needs an analytical Green’s function for each specific PDE and problem domain, making nontrivial exterior boundary conditions complicated to implement. The IB method, on the other hand, does not require a Green’s function and can be used on more general domains. The method we present in this paper maintains the flexibility of the IB method while capturing the better conditioning of a double layer integral equation.

The connection between the IB constraint method and a regularized single layer integral equation has been identified in a few recent works. Usabiaga et al. illustrate this connection and discuss that their rigid multiblob method can be seen as a technique for solving a regularized first-kind integral equation for Stokes flow [39]. Eldredge [40] made a more general connection between IB methods and boundary integral equations by extending the form of a PDE to govern a variable that defines a different function for each side of an immersed boundary. The resulting PDE contains jumps in field quantities across the boundary, which correspond to the strengths of single and double layer potentials. This general connection allows for solutions on either side of the boundary. However, in this work, we look specifically at the IB method for prescribed boundary values for which the PDE domain exists on only one side of the boundary, and we create an IB formulation that corresponds to the use of a double layer potential alone in order to take advantage of the better conditioning.

In this paper, we present an introduction to the new *Immersed Boundary Double Layer (IBDL) method*, as it applies to scalar elliptic PDEs. This is a first step towards applying the method to Stokes and Navier-Stokes flows with rigid bodies, which will be presented in a forthcoming work. The method is able to achieve the same order of accuracy as the original IB constraint method away from the boundary, while only requiring a small number of iterations of a Krylov method. In particular, as we show in the results section, we see iteration counts that range from 10 to 2500 times smaller than those of the

IB constraint method, depending on the domain and boundary value problem. Furthermore, unlike those of the IB constraint method, these iteration counts are essentially independent of the grid point spacing. We derive, implement, and analyze this method for the 2-D Helmholtz and Poisson problems with Dirichlet boundary conditions. With the drastically improved efficiency, the method has the potential to be utilized in moving domains and 3-D problems without the need for stiff parameters or preconditioners. Additionally, while the original constraint method applies only to Dirichlet problems, our new method can also be used for Neumann boundary conditions.

The paper is organized as follows. In Section 2, we give the necessary background material on the IB constraint method and boundary integral methods. In Section 3, we explicitly demonstrate the connection between the IB constraint method and a single layer integral equation. The main contribution of this paper is contained in Section 4, where we formulate the new Immersed Boundary Double Layer method. In Section 5, we discuss the numerical implementation. Section 6 gives the results for the 2-D Helmholtz and Poisson problems with comparisons to the IB constraint method. We also make numerical observations concerning pointwise convergence near the boundary and convergence of the potential strength. Lastly, we end with a discussion in Section 7.

2. Background methods

In order to present our method, we will restrict our attention to the 2-D Dirichlet Helmholtz equation,

$$\Delta u - k^2 u = g \quad \text{in } \Omega \tag{1a}$$

$$u = U_b \quad \text{on } \Gamma, \tag{1b}$$

where Ω is the domain of our PDE, and $\Gamma = \partial\Omega$. We will explore several interior and exterior problem domains for Ω .

Sections 2.1 and 2.2 will discuss two types of methods that can be used to solve this PDE, the Immersed Boundary constraint method and boundary integral equations. The two families of methods will be connected in Section 3 and then used in the formulation of a new scheme in Section 4.

2.1. Immersed Boundary constraint method

One approach for solving Equation (1) is the Immersed Boundary constraint method [19, 20]. In this method, the original PDE domain Ω is embedded into a larger computational domain \mathcal{C} . The method then utilizes a Lagrangian coordinate system located on the immersed boundary, as well as an Eulerian coordinate system, in the form of a regular grid. Figure 1 illustrates these coordinate systems with two possible PDE domains.

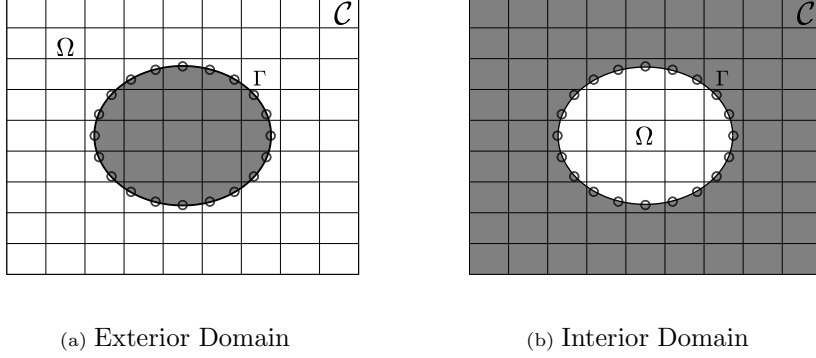


Figure 1: Diagram showing the two IB coordinate systems for an immersed structure Γ , embedded in a 2-D computational domain \mathcal{C} . The physical domain or PDE domain, given by Ω , is shown in white, and the non-physical domain is shown in grey. [1a](#) shows an exterior PDE domain, and [1b](#) shows an interior PDE domain.

In the original IB framework, the density of the force exerted by the structure on the fluid is represented by F , and it is supported on the boundary Γ . F is mapped to the Eulerian grid through a convolution with a delta function. The resulting Eulerian force density is incorporated into the PDE, which is then solved in \mathcal{C} . With the elimination of the physical boundary, the PDE solve can be done efficiently on a regular grid. The resulting solution u can then be mapped back to the boundary through another convolution with a delta function, and this gives the boundary values.

In the case of prescribed boundary values, as in Equation (1), the force density, F , is a Lagrange multiplier, used to enforce the boundary condition. We will use s and \mathbf{x} as our Lagrangian and Eulerian coordinates, respectively. Additionally, $\mathbf{X}(s)$ will be used as a parametrization of the boundary Γ . We then get the following equations for the continuous IB formulation of Equation (1).

$$\Delta \tilde{u}(\mathbf{x}) - k^2 \tilde{u}(\mathbf{x}) + \int_{\Gamma} F(s) \delta(\mathbf{x} - \mathbf{X}(s)) ds = \tilde{g}(\mathbf{x}) \quad \text{in } \mathcal{C} \quad (2a)$$

$$\int_{\mathcal{C}} \tilde{u}(\mathbf{x}) \delta(\mathbf{x} - \mathbf{X}(s)) d\mathbf{x} = U_b(s) \quad \text{on } \Gamma \quad (2b)$$

In the above formulation, our unknowns are F and \tilde{u} . Note that $\tilde{u}(\mathbf{x})$ and $\tilde{g}(\mathbf{x})$ represent extensions of the solution u and the function g from Ω to the larger computational domain \mathcal{C} . Once the solution $\tilde{u}(\mathbf{x})$ is found in \mathcal{C} , the solution to the original PDE is then given by $\tilde{u}|_{\Omega}$. As such, we will drop the tilde notation on $u(x)$. On the other hand, we can define the extension of g by $\tilde{g} = g\chi_{\Omega} + g_e\chi_{\mathcal{C}\setminus\Omega}$, where χ is an indicator function. Since $\mathcal{C} \setminus \Omega$ is not in the PDE domain, there is flexibility in our choice for g_e . For example, we can simply use a smooth extension of g or use $g_e = 0$.

For mappings between the coordinate systems, the IB method uses a regularized delta function, δ_h , where the regularization lengthscale, h , is generally chosen to be on the order of grid point spacing. We can then view the first convolution as *spreading* the force density to the nearby grid points, and the second convolution as *interpolating* the solution values onto the boundary points. Therefore, let us define the spread and interpolation operators, respectively, as

$$(SF)(\mathbf{x}) = \int_{\Gamma} F(s)\delta_h(\mathbf{x} - \mathbf{X}(s))ds \quad (3a)$$

$$(S^*u)(s) = \int_{\mathcal{C}} u(\mathbf{x})\delta_h(\mathbf{x} - \mathbf{X}(s))d\mathbf{x}. \quad (3b)$$

These operators are adjoint in the sense that

$$\langle SF, u \rangle_{\mathcal{C}} = \langle F, S^*u \rangle_{\Gamma}, \quad (4)$$

where the inner products are the usual L^2 inner products on Ω and Γ , respectively. Discretization and numerical implementation will be discussed more in Section 5, but note that we will also use S and S^* to refer to the discretized versions of these operators. Similarly, let \mathcal{L} represent our continuous or discretized Helmholtz operator. We then get the following system of equations.

$$\mathcal{L}u + SF = \tilde{g} \quad \text{in } \mathcal{C} \quad (5a)$$

$$S^*u = U_b \quad \text{on } \Gamma, \quad (5b)$$

or

$$\begin{pmatrix} \mathcal{L} & S \\ S^* & 0 \end{pmatrix} \begin{pmatrix} u \\ F \end{pmatrix} = \begin{pmatrix} \tilde{g} \\ U_b \end{pmatrix}. \quad (6)$$

We can solve this saddle point problem by first solving the equation

$$-(S^*\mathcal{L}^{-1}S)F = U_b - S^*\mathcal{L}^{-1}\tilde{g} \quad (7)$$

for F by inverting the Schur complement and then obtaining u from Equation (5a).

However, generically these saddle point problems resulting from Dirichlet boundary conditions are poorly conditioned [41]. For example, for the 3-D Stokes equation with a spherical immersed boundary, Kallemov et al. found that the condition number grows linearly in the number of immersed boundary points, for $\Delta s \geq \Delta x$ [20]. Furthermore, as Δs is decreased, the increase in condition number is rapid, resulting in an inability to solve the system in double-precision arithmetic for $\Delta s \approx 0.5\Delta x$ [20]. Figure 2 gives the condition numbers for the Schur complement and the subsequent iteration counts of `minres`¹ needed for solving Equation (7) without preconditioning, where $k = 1$

¹We utilize `minres` from MATLAB R2022a [42].

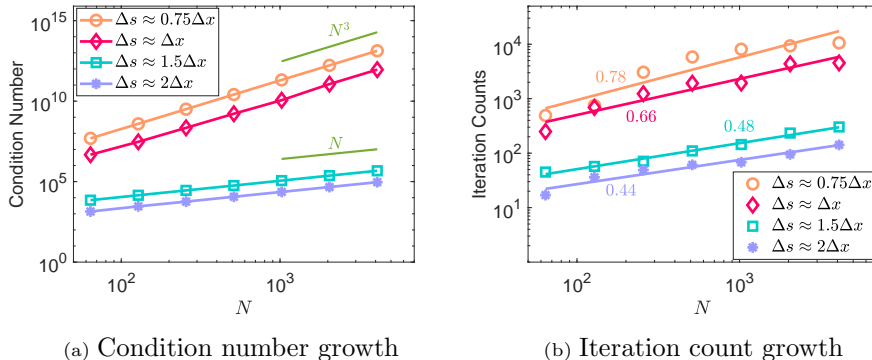


Figure 2: Condition numbers and iteration counts for the solution of Equation (7) with $k = 1$ and $g = 0$ on the periodic computational domain $[-0.5, 0.5]^2$, where the circular boundary of radius 0.25 has prescribed boundary values given by $U_b = \sin 2\theta$. 2a gives the condition number of the Schur complement, given by the left-hand-side of Equation (7) for various values of N , the number of grid points in one direction and for various immersed boundary point spacings. 2b gives the subsequent number of iterations of `minres`, with tolerance 10^{-8} , needed to solve the system, along with the best-fit lines, labeled with their slopes.

and Γ is a circle. As will be discussed in Section 5, our computational domain is a periodic box, and we use a finite difference method for discretizing the Helmholtz operator. This PDE will be revisited in Section 6.1. We can see that for wider boundary point spacing, the condition number grows as $\mathcal{O}(N)$, where N is the number of grid points in one direction. For tighter boundary point spacings, we see the condition numbers grow even more rapidly, as $\mathcal{O}(N^3)$. The subsequent iteration counts for this problem grow between $\mathcal{O}(\sqrt{N})$ and $\mathcal{O}(N)$. With an eye toward time-dependent PDE in applications such as fluid dynamics, where this system would be solved in each time step, these iteration counts can be prohibitively large without proper preconditioning. Therefore, as mentioned in the introduction, much work has been devoted to forming preconditioners [20, 29, 30, 31]. However, preconditioning itself can be computationally expensive, as it often involves inverting a dense matrix. In Section 4, we present an alternative IB formulation that achieves the same order of accuracy as this constraint method while avoiding these high iteration counts and therefore eliminating the need for preconditioning.

2.2. Integral methods

Boundary integral methods can also be used to solve Equation (1) by reformulating the boundary value problem as an integral equation, using the appropriate Green's function [34]. The Green's function for this PDE satisfies

$$\Delta G(\mathbf{x}, \mathbf{x}_0) - k^2 G(\mathbf{x}, \mathbf{x}_0) = -\delta(\mathbf{x} - \mathbf{x}_0) \quad \text{in } \Omega. \quad (8)$$

For convenience, let $g = 0$, and let our problem domain Ω be an interior domain, with boundary Γ . Similar steps can be taken for an exterior domain.

First, Green's second identity simplifies for this PDE to

$$u(\mathbf{x})\delta(\mathbf{x} - \mathbf{x}_0) = \nabla \cdot \left(G(\mathbf{x}, \mathbf{x}_0)\nabla u(\mathbf{x}) - u(\mathbf{x})\nabla G(\mathbf{x}, \mathbf{x}_0) \right). \quad (9)$$

Let $\mathbf{x}_0 \in \Gamma$. Then by integrating Equation (9) over Ω and using the divergence theorem, we get the integral representation of u ,

$$u(\mathbf{x}_0) = \int_{\Gamma} G(\mathbf{x}, \mathbf{x}_0)\nabla u(\mathbf{x}) \cdot \mathbf{n}(\mathbf{x})dl(\mathbf{x}) - \int_{\Gamma} u(\mathbf{x})\nabla G(\mathbf{x}, \mathbf{x}_0) \cdot \mathbf{n}(\mathbf{x})dl(\mathbf{x}), \quad (10)$$

where \mathbf{n} is the unit normal of Γ , pointing out of Ω . We use $dl(\mathbf{x})$ to denote an integral with respect to arclength.

The first term of Equation (10) is called a *single layer potential*, which can be viewed as a distribution of point sources on the boundary, and the second term is called a *double layer potential*, which can be viewed as a distribution of point source dipoles on the boundary. Notice that the strength of the single layer potential is given by the boundary distribution of the normal derivative of u , and the strength of the double layer potential is given by the boundary values of u .

There are, however, other integral representations of the solution u in Ω . We can, for instance, represent u solely with a single layer potential or a double layer potential. Let us consider two solutions: u^{Int} that satisfies the PDE on Ω and u^{Ext} that satisfies the PDE on Ω^{Ext} , the region exterior to Γ . Let these two solutions share the same values on Γ . In order to find a single layer representation for $u^{Int}(\mathbf{x}_0)$ for $\mathbf{x}_0 \in \Omega$ we need two equations. Firstly, we use Equation (10) for u^{Int} . Secondly, by the same process that gave us Equation (10), we can get a similar equation for u^{Ext} , where the corresponding normal vector points outward from Ω^{Ext} , and the left-hand side vanishes because $\mathbf{x}_0 \notin \Omega^{Ext}$. By negating the expression in order to use the same unit normal as that in Equation (10), we get the following equation for u^{Ext} :

$$0 = - \int_{\Gamma} G(\mathbf{x}, \mathbf{x}_0)\nabla u^{Ext}(\mathbf{x}) \cdot \mathbf{n}(\mathbf{x})dl(\mathbf{x}) + \int_{\Gamma} u^{Ext}(\mathbf{x})\nabla G(\mathbf{x}, \mathbf{x}_0) \cdot \mathbf{n}(\mathbf{x})dl(\mathbf{x}). \quad (11)$$

Then, by adding Equation (10), for u^{Int} , and Equation (11), we get the *generalized single layer integral representation* for u^{Int} given by

$$u^{Int}(\mathbf{x}_0) = \int_{\Gamma} \sigma(\mathbf{x})G(\mathbf{x}, \mathbf{x}_0)dl(\mathbf{x}), \quad (12)$$

where $\sigma = \nabla(u^{Int} - u^{Ext}) \cdot \mathbf{n} \Big|_{\Gamma}$ is the strength of the single layer potential.

If we instead consider two such solutions which match normal derivatives on the boundary, we get the *generalized double layer integral representation* for

u^{Int} given by

$$u^{Int}(\mathbf{x}_0) = \int_{\Gamma} \gamma(\mathbf{x}) \nabla G(\mathbf{x}, \mathbf{x}_0) \cdot \mathbf{n}(\mathbf{x}) dl(\mathbf{x}), \quad (13)$$

where $\gamma = (u^{Ext} - u^{Int})|_{\Gamma}$ is the strength of the double layer potential.

In order to use our boundary data, we then take $\mathbf{x}_0 \rightarrow \Gamma$. To have consistent notation across methods, we will denote a boundary point with a capital letter, \mathbf{X}_0 . Then, to generalize for exterior domains, we emphasize again that \mathbf{n} is the unit normal pointing out of Ω , regardless of whether Ω is an exterior or interior domain. Using our boundary condition, Equations (12) and (13) give us

$$U_b(\mathbf{X}_0) = \int_{\Gamma} \sigma(\mathbf{x}) G(\mathbf{x}, \mathbf{X}_0) dl(\mathbf{x}), \quad (14)$$

$$U_b(\mathbf{X}_0) = \int_{\Gamma}^{PV} \gamma(\mathbf{x}) \nabla G(\mathbf{x}, \mathbf{X}_0) \cdot \mathbf{n}(\mathbf{x}) dl(\mathbf{x}) - \frac{1}{2} \gamma(\mathbf{X}_0), \quad (15)$$

where PV denotes the principal-value integral, for which \mathbf{X}_0 is placed exactly on Γ . It is computed by integrating over $\Gamma \setminus B_{\epsilon}(\mathbf{X}_0)$, in which a disk around \mathbf{X}_0 has been removed from the boundary. The PV integral then comes from taking the limit as ϵ goes to 0. The $1/2$ in Equation (15) is obtained using the properties of the normal derivative of the Green's function. For a reference, see Section 2.4 in [34].

The unknown quantities in Equations (14) and (15) are the potential strengths, σ and γ , respectively. Equation (14) has the form of a Fredholm integral of the first kind, and Equation (15) has the form of a Fredholm integral of the second kind [43]. The operators given by

$$K_1 \sigma = \int_{\Gamma} \sigma(\mathbf{x}) G(\mathbf{x}, \mathbf{x}_0) dl(\mathbf{x}) \quad (16a)$$

$$K_2 \gamma = \int_{\Gamma} \gamma(\mathbf{x}) \nabla G(\mathbf{x}, \mathbf{x}_0) \cdot \mathbf{n}(\mathbf{x}) dl(\mathbf{x}) \quad (16b)$$

have eigenvalues in the interval $(-0.5, 0.5)$, and the only limit point of the eigenvalues is 0. [44, 45]. The condition number, defined as the ratio of the largest and smallest eigenvalues, is therefore infinite in the continuous case and large in the discretized case. On the other hand, Equation (15) can be rewritten as

$$\left(K_2 - \frac{1}{2}I\right)\gamma = U_b, \quad (17)$$

where I is the identity operator. Shifting the operator in this way shifts the eigenvalues, and the only limit point for the eigenvalues becomes $-1/2$. Therefore, the condition number of the discretized operator is finite and does not grow with refinement of the discretization. The better conditioning of this operator is the characteristic of the double layer representation that we exploit to form our new Immersed Boundary method.

3. Connection between IB method and integral methods

In this section, we relate the Immersed Boundary constraint method as described in Section 2.1 to the single layer integral equation in Equation (14). As discussed in Section 1, this connection has been established in several recent works [39, 40], but here, we present this connection explicitly from the IB constraint system of Equation (5). After establishing this connection between the two types of methods, we propose that a solution to the conditioning problem of the Schur complement seen in Equation (7) is to formulate an Immersed Boundary version of a double layer integral equation. Such a formulation will be presented in Section 4.

For Sections 3 and 4, we will simplify the presentation by focusing on the homogeneous case, or $g = 0$. However, this connection holds for the inhomogeneous case as well, and we use the new method on several inhomogeneous problems in Section 6.

Let us define a regularized Green's function by

$$G_h(\mathbf{x}, \mathbf{x}_0) \equiv G * \delta_h = \int_{\mathcal{C}} G(\mathbf{y}, \mathbf{x}_0) \delta_h(\mathbf{x} - \mathbf{y}) d\mathbf{y}. \quad (18)$$

The linearity of our operator then gives us that

$$\mathcal{L}G_h(\mathbf{x}, \mathbf{x}_0) = -\delta_h(\mathbf{x} - \mathbf{x}_0). \quad (19)$$

The homogeneous IB constraint equations are given by

$$\mathcal{L}u + SF = 0 \quad \text{in } \mathcal{C} \quad (20a)$$

$$S^*u = U_b \quad \text{on } \Gamma. \quad (20b)$$

Starting with the first equation of the IB constraint method, Equation (20a), we have

$$\mathcal{L}u = -SF = - \int_{\Gamma} F(s) \delta_h(\mathbf{x} - \mathbf{X}(s)) ds. \quad (21)$$

Inverting the operator and using Equation (19), we get

$$u(\mathbf{x}) = \int_{\Gamma} F(s) G_h(\mathbf{x}, \mathbf{X}(s)) ds \quad (22)$$

for $\mathbf{x} \in \Omega \setminus \Gamma$. The second equation of the IB constraint method, Equation (20b), gives us

$$U_b(s') = \int_{\mathcal{C}} u(\mathbf{x}) \delta_h(\mathbf{x} - \mathbf{X}(s')) dx, \quad (23)$$

where we are using s' to distinguish from our previous variable of integration or alternately, viewing $\mathbf{X}(s')$ as selecting a particular boundary point. Combining this with Equation (22) and changing the order of integration, we get

$$U_b(s') = \int_{\Gamma} F(s) \int_{\mathcal{C}} G_h(\mathbf{x}, \mathbf{X}(s)) \delta_h(\mathbf{x} - \mathbf{X}(s')) d\mathbf{x} ds. \quad (24)$$

Notice that the second integral is equivalent to $G_h * \delta_h$, evaluated at $\mathbf{X}(s')$. Therefore, by denoting a twice-regularized Green's function by G_{hh} , this becomes

$$U_b(s') = \int_{\Gamma} F(s) G_{hh}(\mathbf{X}(s'), \mathbf{X}(s)) ds. \quad (25)$$

The symmetry of the Green's function, which is preserved through convolutions with the regularized delta function, gives us that $G_{hh}(\mathbf{X}(s'), \mathbf{X}(s)) = G_{hh}(\mathbf{X}(s), \mathbf{X}(s'))$. Using this to switch the arguments of G_{hh} and appropriately redefining F and U_b as functions of \mathbf{x} , we get

$$U_b(\mathbf{X}(s')) = \int_{\Gamma} F(\mathbf{X}(s)) G_{hh}(\mathbf{X}(s), \mathbf{X}(s')) ds. \quad (26)$$

Recall that the single layer integral equation for \mathbf{X}_0 on the boundary is given by

$$U_b(\mathbf{X}_0) = \int_{\Gamma} \sigma(\mathbf{x}) G(\mathbf{x}, \mathbf{X}_0) dl(\mathbf{x}). \quad (27)$$

By parametrizing Γ by $\mathbf{X}(s)$, this becomes

$$U_b(\mathbf{X}(s')) = \int_{\Gamma} \sigma(\mathbf{X}(s)) G(\mathbf{X}(s), \mathbf{X}(s')) \left| \frac{\partial \mathbf{X}(s)}{\partial s} \right| ds. \quad (28)$$

By comparing Equations (26) and (28), we can associate the IB constraint force F with the potential strength modified by the parametrization term, $|\partial \mathbf{X}(s)/\partial s|$. In other words, in the limit that the regularization width, h , approaches 0, we have

$$F(\mathbf{X}) = \sigma(\mathbf{X}) \left| \frac{\partial \mathbf{X}}{\partial s} \right|. \quad (29)$$

Specifically, in the case of an arclength parametrization, where $|\partial \mathbf{X}(s)/\partial s| = 1$, we see from Section 2.2 that F gives the jump in the normal derivative of the solution across the boundary. We have now established that the IB constraint method is equivalent to a *regularized* single layer integral equation. As such, in order to distinguish it from the new method we propose in Section 4, we will henceforth refer to this as the Immersed Boundary Single Layer (IBSL) method.

4. The Immersed Boundary Double Layer (IBDL) method

4.1. Formulation of the IBDL method

The discussion at the end of Section 2.2 suggests that to improve the conditioning of the IBSL method, we could use an Immersed Boundary framework to instead solve a regularized *double* layer integral equation, which has better conditioning. We will call this the Immersed Boundary Double Layer (IBDL) method, and it is given by

$$\mathcal{L}u + \tilde{S}Q = \tilde{g} \quad \text{in } \mathcal{C} \quad (30a)$$

$$S^*u + \frac{1}{2}Q = U_b \quad \text{on } \Gamma, \quad (30b)$$

where we assume an arclength parametrization of Γ , and where $\tilde{S}Q \equiv \nabla \cdot (SQ\mathbf{n})$ for \mathbf{n} , the unit normal on Γ , pointing out of Ω . The form of \tilde{S} implies that Q gives the strength of a dipole force distribution on the boundary, and this is our Lagrange multiplier used to enforce the boundary condition. We will next demonstrate that this formulation corresponds to a double layer integral equation.

Starting with the Equation (30a), and taking $g = 0$ for simplicity, we have

$$\mathcal{L}u = -\tilde{S}Q = -\nabla \cdot \int_{\Gamma} Q(s)\mathbf{n}(s)\delta_h(\mathbf{x} - \mathbf{X}(s))ds. \quad (31)$$

Inverting the operator and using Equation (19), we get

$$u(\mathbf{x}) = \nabla \cdot \int_{\Gamma} Q(s)\mathbf{n}(s)G_h(\mathbf{x}, \mathbf{X}(s))ds \quad (32)$$

for $\mathbf{x} \in \Omega \setminus \Gamma$. Bringing in the divergence and manipulating the expression, we get

$$u(\mathbf{x}) = \int_{\Gamma} Q(s)\nabla G_h(\mathbf{x}, \mathbf{X}(s)) \cdot \mathbf{n}(s)ds. \quad (33)$$

Then, the second equation of the IBDL method, Equation (30b), gives us

$$U_b(s') = \int_{\mathcal{C}} u(\mathbf{x})\delta_h(\mathbf{x} - \mathbf{X}(s'))dx + \frac{1}{2}Q(s'). \quad (34)$$

Combining Equation (33) with Equation (34), changing the order of integration, and again recognizing the presence of $G_{hh} = G_h * \delta_h$, we get

$$U_b(s') = \int_{\Gamma} Q(s)\nabla G_{hh}(\mathbf{X}(s'), \mathbf{X}(s)) \cdot \mathbf{n}(s)ds + \frac{1}{2}Q(s'). \quad (35)$$

The odd symmetry of the gradient of the Green's function [34], which is again preserved through the convolutions with the regularized delta function, gives us that $\nabla G_{hh}(\mathbf{X}(s'), \mathbf{X}(s)) = -\nabla G_{hh}(\mathbf{X}(s), \mathbf{X}(s'))$. Using this to switch the arguments of ∇G_{hh} and appropriately redefining Q and U_b as functions of \mathbf{x} , we get

$$U_b(\mathbf{X}(s')) = - \int_{\Gamma} Q(\mathbf{X}(s)) \nabla G_{hh}(\mathbf{X}(s), \mathbf{X}(s')) \cdot \mathbf{n}(\mathbf{X}(s)) ds + \frac{1}{2} Q(\mathbf{X}(s')). \quad (36)$$

Recall that the double layer integral equation for \mathbf{X}_0 on the boundary is given by

$$U_b(\mathbf{X}_0) = \int_{\Gamma}^{\text{PV}} \gamma(\mathbf{x}) \nabla G(\mathbf{x}, \mathbf{X}_0) \cdot \mathbf{n}(\mathbf{x}) dl(\mathbf{x}) - \frac{1}{2} \gamma(\mathbf{X}_0). \quad (37)$$

Using our arclength parametrization, we can rewrite this as

$$U_b(\mathbf{X}(s')) = \int_{\Gamma}^{\text{PV}} \gamma(\mathbf{X}(s)) \nabla G(\mathbf{X}(s), \mathbf{X}(s')) \cdot \mathbf{n}(\mathbf{X}(s)) ds - \frac{1}{2} \gamma(\mathbf{X}(s)). \quad (38)$$

By comparing Equations (36) and (38), we see that in the limit that the regularization width, h , approaches 0, we have

$$Q(\mathbf{X}) = -\gamma(\mathbf{X}). \quad (39)$$

Therefore, we can see that the IBDL method is equivalent to a *regularized* double layer integral equation. Note from Section 2.2 that Q gives the jump in the solution across the boundary.

We reiterate that the formulation, specifically Equation (30b), assumes that $\mathbf{X}(s)$ gives an arclength parametrization of Γ . In the IBSL method, if we use a different parametrization of the boundary, the rescaling of F seen in Equation (29) accounts for the transformation, and no alteration in the method is needed to find the solution. However, in the IBDL method, since the $1/2$ in Equation (30b) is derived using an arclength parametrization, one would need to alter this term in the case that $|\partial \mathbf{X}(s)/\partial s| \neq 1$. This will be discussed further in Section 4.3, but otherwise, we will assume an arclength parametrization throughout this paper.

4.2. Discontinuity of the solution

Since our boundary density Q corresponds to the jump in the solution values across the boundary, clearly our solution u will be discontinuous. In the original IB constraint method, the solution was continuous, but the normal derivative was not. Figure 3 illustrates the solutions to Equation (1) produced by the IBSL and IBDL methods on the entire computational domain, $\mathcal{C} = [-0.5, 0.5]^2$. The PDE domain Ω is the interior of a circle, and the boundary condition is

$U_b = e^x$. We use the numerical implementation discussed in Section 5. We can see that the two solutions match on the portion of the problem domain, Ω , that is about a couple meshwidths away from the boundary. However, the IBDL method gives a solution that is discontinuous across the boundary.

The lack of smoothness in the derivative across the boundary causes the IBSL method to achieve only first-order accuracy. Since the IBDL method will instead yield a discontinuous function, we will not see pointwise convergence near the boundary if we use the solution values given directly from the method in Equation (30). However, we do achieve first-order convergence in all norms in the region away from the boundary by a distance that is $\mathcal{O}(\Delta x)$. If we then wish to recover pointwise convergence up to the boundary, we can replace the values of u for grid points *near* the boundary.

Integral equation methods are generally able to achieve higher accuracy than the Immersed Boundary method. However, this lack of smoothness related to the singularity in the Green’s function derivative results in the need to employ analytical techniques in order to achieve the same level of accuracy for points near Γ . For instance, Beale and Lai use a regularized Green’s function and then analytically derive the correction terms [46]. Klöckner et al. use analytic expansions centered at points several meshwidths from the boundary to evaluate the solution at points nearer to the boundary [47], and Carvalho et al. use asymptotic analysis to approximate the solution at near-boundary points with known boundary data and a nonlocal correction [36].

For problems involving prescribed boundary values on sharp interfaces, the lack of smoothness of a solution from an IB method generically results in only first-order accuracy. While higher-order accuracy has been possible on problems with smooth solutions across the boundary [48, 49, 50, 31], here we are restricting our attention to achieving the pointwise first-order convergence achieved by the IBSL method applied to a sharp interface. Therefore, while there are many options for replacing the solution values near the boundary, we have chosen to use a simple linear interpolation because with this choice, we are able to obtain the first-order accuracy desired. This interpolation uses known boundary values and approximate solution values several meshwidths into the PDE domain. [Appendix A](#) provides details of the numerical implementation.

There are two regions of grid points for which we do not see pointwise convergence. The first region contains the largest errors, and it is illustrated in Figure 4 for an interior circular domain with boundary data $U_b = e^x$. We can see that this region remains localized to only a small number of grid points, so that as we refine the grid, the width of this region quickly goes to 0. These large errors are the direct result of the smoothing of the dipole forces, and the number of meshwidths is therefore determined by the support of the regularized delta function used. As we discuss in Section 5, we use the traditional Peskin four-point delta function in Equations (58)-(59) [2], and this results in about 2 – 3 meshwidths of large errors on one side of the boundary, which can be

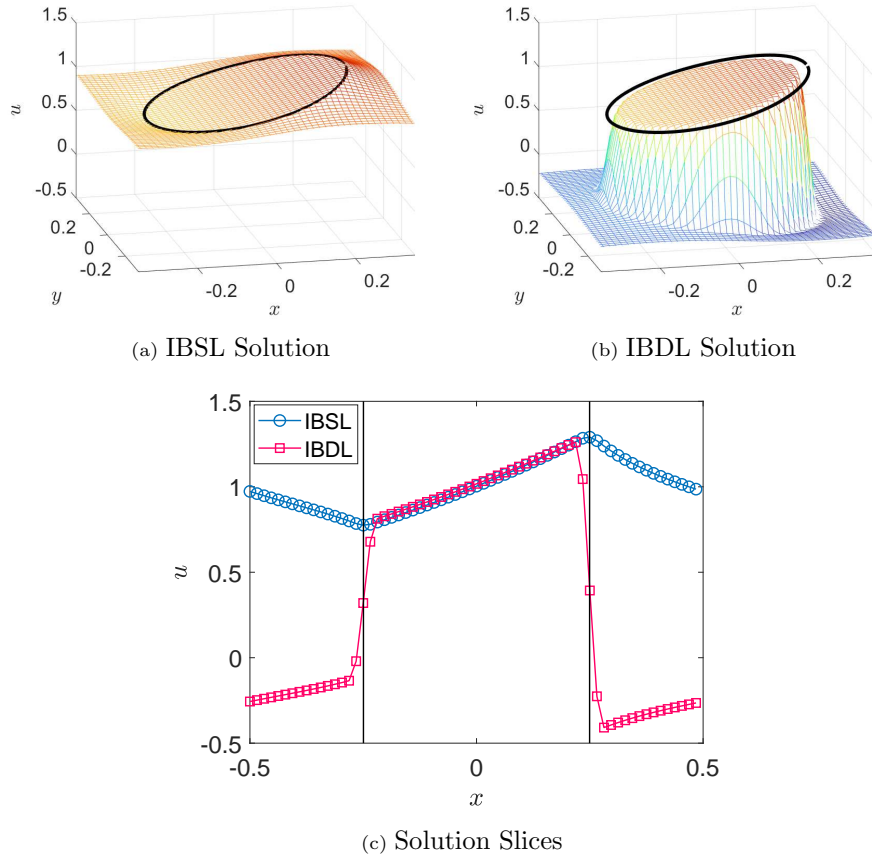


Figure 3: Solution plots found using the IBSL and IBDL methods to solve Equation (1) with $k = 1$ and $g = 0$, and where the circular boundary of radius 0.25 has prescribed boundary values given by $U_b = e^x$. The periodic computational domain is $[-0.5, 0.5]^2$, and the grid and boundary point spacing is $\Delta s \approx \Delta x = 2^{-6}$. Figure 3a gives the solution from using the IBSL method, and Figure 3b, the IBDL method. U_b is shown with a black curve. Figure 3c shows solution values for $y = -0.015625$ for both methods, and the black vertical lines show the location of the immersed boundary.

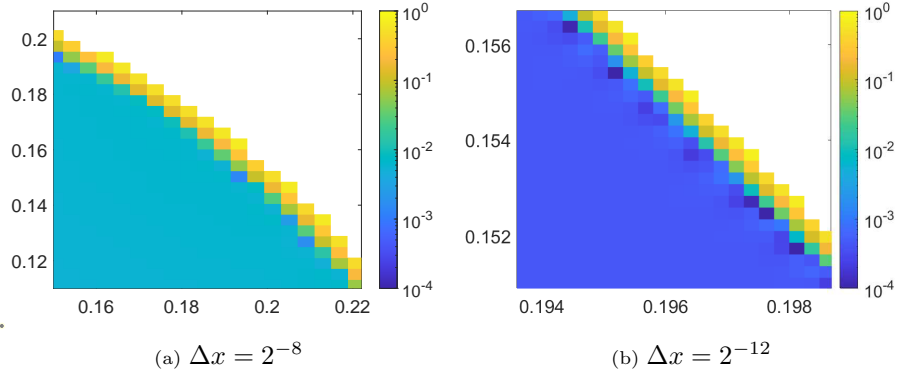


Figure 4: Plots of errors from using IBDL method to solve Equation (1) with $k = 1$ and $g = 0$ on the periodic computational domain $[-0.5, 0.5]^2$, where the circular boundary of radius 0.25 has prescribed boundary values given by $U_b = e^x$. The errors are shown for two grid point spacings and with $\Delta s \approx \Delta x$. The figure is zoomed-in to view the large errors that lie in a small region near Γ .

seen in Figure 4.

Secondly, the numerical method used to discretize the PDE spreads the error from the discontinuity into a larger region near the boundary. Therefore, if we use the interpolation to only correct for the large errors within the first few meshwidths, we will still see a lessening of first-order convergence in the max norm once the max norm is small enough. The width of the region on which the solution fails to converge pointwise still approaches 0, but the number of meshwidths affected can increase. We can recover pointwise convergence with further interpolation, and in practice, we can generally obtain a comparable maximum error to the IBSL method by using interpolation for only a relatively small number of meshwidths. In Section 6.2, we further discuss factors that contribute to the number of meshwidths needed.

The IBDL method can now be described in the following steps:

1. Use a Krylov method to solve the following system for Q .

$$-(S^* \mathcal{L}^{-1} \tilde{S})Q + \frac{1}{2}Q = U_b - S^* \mathcal{L}^{-1} \tilde{g} \quad (40)$$

2. Use Q to solve the following equation for u in \mathcal{C} .

$$\mathcal{L}u + \tilde{S}Q = \tilde{g} \quad (41)$$

3. Use an interpolation to replace the values for u at $\mathbf{x} \in \Omega$ that are near Γ . Factors that determine the number of meshwidths to include in this step are discussed in Section 6.2. Note: This step is *optional*, and only required if we wish to recover pointwise convergence *up to the boundary*.

4.3. Arbitrary boundary parametrization

In this paper, we utilize an arclength parametrization of the immersed boundary Γ . Numerically, this means that in the discretization of the spread operator, Δs_i is the size of the arclength connecting $\mathbf{X}(s_i)$ and $\mathbf{X}(s_{i+1})$. In practice, this choice is not a limiting factor because even if an analytical arclength parametrization of the immersed boundary curve is not available, we can still approximate this value with the distance $\Delta s_i \approx \|\mathbf{X}(s_{i+1}) - \mathbf{X}(s_i)\|_2$. However, to be thorough, in this section, we discuss the use of an arbitrary parametrization.

Let $\mathbf{X}(s)$ be an arbitrary smooth parametrization of Γ . Using this parametrization, the double layer integral equation for the Helmholtz equation would have the form

$$U_b(\mathbf{X}(s')) = \int_{\Gamma}^{PV} \gamma(\mathbf{X}(s)) \nabla G(\mathbf{X}(s), \mathbf{X}(s')) \cdot \mathbf{n}(\mathbf{X}(s)) \left| \frac{\partial \mathbf{X}}{\partial s} \right| ds - \frac{1}{2} \gamma(\mathbf{X}(s')). \quad (42)$$

In this case, we can form the IBDL method as

$$\mathcal{L}u + \tilde{S}Q = \tilde{g} \quad \text{in } \mathcal{C} \quad (43a)$$

$$S^*u + \frac{1}{2|\partial \mathbf{X}/\partial s|} Q = U_b \quad \text{on } \Gamma. \quad (43b)$$

Then, using the same steps as in Section 4.1, we would obtain the equation

$$U_b(\mathbf{X}(s')) = - \int_{\Gamma}^{PV} Q(\mathbf{X}(s)) \nabla G_{hh}(\mathbf{X}(s), \mathbf{X}(s')) \cdot \mathbf{n}(\mathbf{X}(s)) ds + \frac{1}{2|\partial \mathbf{X}/\partial s|} Q(\mathbf{X}(s')). \quad (44)$$

By comparing Equations (42) and (44), we see that in the limit $h \rightarrow 0$, we get

$$Q(\mathbf{X}) = -\gamma(\mathbf{X}) \left| \frac{\partial \mathbf{X}}{\partial s} \right|. \quad (45)$$

As discussed in Section 2.2, the constant 1/2 shifts all of the eigenvalues of the integral operator so that the only limit point is away from 0. This ensures a small, constant condition number as the mesh is refined and therefore small iteration counts for the Krylov method. An arbitrary parametrization may not shift the eigenvalues in this uniform manner. As such, the iteration counts may increase. In Section 6.1, we revisit the Helmholtz equation from Section 2.1 given by

$$\Delta u - u = 0 \quad \text{in } \Omega \quad (46a)$$

$$u = \sin 2\theta \quad \text{on } \Gamma, \quad (46b)$$

where Ω is the interior of a circle of radius 0.25, centered at the origin. We will see that the iteration count for solving this equation with the IBDL method using arclength parametrization is about 4-5 iterations. If we instead use the parametrization given by

$$\begin{pmatrix} x \\ y \end{pmatrix} = \begin{pmatrix} 0.25 \cos(s^2 + s) \\ 0.25 \sin(s^2 + s) \end{pmatrix}, \quad (47)$$

for $0 \leq s \leq \frac{1}{2}(-1 + \sqrt{1 + 8\pi})$, we have

$$\left| \frac{\partial \mathbf{X}}{\partial s} \right| = 0.25(2s + 1). \quad (48)$$

Using immersed boundary points that are equally spaced in the parameter s , the iteration count is about 20. The iteration count is larger, but it does remain constant as the mesh is refined. This is likely to be the case with an arbitrary parametrization as the eigenvalues will still be shifted in some manner away from 0. It is therefore acceptable to implement the IBDL method in this manner, but we then need the values or approximations of $|\partial \mathbf{X} / \partial s|$. To maintain consistency in the formulation of the IBDL method, we will use an arclength parametrization, with equally spaced points, in all other sections of this paper.

4.4. Neumann boundary conditions

We now use the IB framework and our connection to boundary integral equations to solve a PDE with Neumann boundary conditions. The original IBSL method was unable to handle such a problem since the derivatives are not convergent at the boundary.

Let us look at the PDE given by

$$\Delta u - k^2 u = g \quad \text{in } \Omega \quad (49a)$$

$$\frac{\partial u}{\partial n} = V_b \quad \text{on } \Gamma, \quad (49b)$$

where we will first take $g = 0$ for simplicity. In Section 2.2, we introduced the full integral representation of u . For $\mathbf{x}_0 \in \Omega \setminus \Gamma$, we have

$$u(\mathbf{x}_0) = \int_{\Gamma} \nabla u(\mathbf{x}) \cdot \mathbf{n}(\mathbf{x}) G(\mathbf{x}, \mathbf{x}_0) dl(\mathbf{x}) - \int_{\Gamma} u(\mathbf{x}) \nabla G(\mathbf{x}, \mathbf{x}_0) \cdot \mathbf{n}(\mathbf{x}) dl(\mathbf{x}). \quad (50)$$

The first term in Equation (50) is a single layer potential with the strength given by the known boundary derivatives, V_b . The second term is a double layer potential whose strength is given by the *unknown* boundary values. If we let $U_b \equiv u|_{\Gamma}$, we can then write the PDE in the IB framework as

$$\mathcal{L}u + \tilde{S}U_b + SV_b = 0 \quad (51)$$

To determine the interpolation equation, we can take $\mathbf{x}_0 \rightarrow \Gamma$ in Equation (50) and denote it as \mathbf{X}_0 . Using the same property of the Green's function derivative that was used in Section 2.2, we get

$$u(\mathbf{X}_0) = \int_{\Gamma} \nabla u(\mathbf{x}) \cdot \mathbf{n}(\mathbf{x}) G(\mathbf{x}, \mathbf{X}_0) dl(\mathbf{x}) - \int_{\Gamma}^{PV} u(\mathbf{x}) \nabla G(\mathbf{x}, \mathbf{X}_0) \cdot \mathbf{n}(\mathbf{x}) dl(\mathbf{x}) + \frac{1}{2} u(\mathbf{X}_0). \quad (52)$$

By combining the $u(\mathbf{X}_0)$ terms, we can identify that the interpolated solution values will correspond to $1/2u(\mathbf{X}_0)$. Allowing for a non-zero g , we can therefore write the PDE in the Immersed Boundary framework as

$$\mathcal{L}u + \tilde{S}U_b + SV_b = \tilde{g} \quad \text{in } \mathcal{C} \quad (53a)$$

$$S^*u = \frac{1}{2}U_b \quad \text{on } \Gamma. \quad (53b)$$

For Neumann boundary conditions, U_b is the *unknown* potential strength on the boundary, corresponding to the unknown boundary values. A detailed demonstration of the connection between Equation (52) and Equation (53) is presented in Appendix B, and it uses steps similar to those used in Sections 3 and 4.1.

We can solve this system by first solving the equation

$$(-S^* \mathcal{L}^{-1} \tilde{S})U_b - \frac{1}{2}U_b = S^* \mathcal{L}^{-1} SV_b - S^* \mathcal{L}^{-1} \tilde{g} \quad (54)$$

for the boundary values, U_b , and then obtaining u from Equation (53a). We can see by comparing to Equation (40) that the operator is similar to that of the IBDL method for Dirichlet boundary conditions, where the only difference is the sign on the $1/2$. Therefore, we again get a well-conditioned problem that can be solved with a small number of iterations of a Krylov method. An example of a Neumann problem will be presented in Section 6.6.

5. Numerical implementation

5.1. Discretization of space and differential operators

In this paper, we take the computational domain to be a periodic box of length L in order to make use of efficient finite difference and Fourier spectral methods to solve Equation (41). As is typical for IB methods, there is flexibility in the choice of PDE solver. However, as is discussed in Section 6.2, the discontinuity of the solution affects the accuracy near the boundary differently for different discretizations of the PDE. Therefore, we use a finite difference method for all applications other than those presented to compare methods in Section 6.2. We use the standard five-point, second-order accurate approximation for the Laplacian.

The computational domain is discretized with a regular Cartesian mesh with N points in each direction, giving us $\Delta x = \Delta y = L/N$. To discretize the boundary, we use a set of N_{IB} boundary points, given by $\{X(s_i)\}_{i=1}^{N_{IB}}$.

5.2. Discretization of spread and interpolation operators

We will first discuss the implementation of our operator defined by

$$\tilde{S}Q = \nabla \cdot (SQ\mathbf{n}). \quad (55)$$

This operation consists of first multiplying our discretized boundary density Q by the outward unit normal vectors at the immersed boundary points, whose locations will be discussed more in depth shortly. We then spread these vectors to the grid and take the divergence. We discuss the implementation of each of these steps below.

The first component of the operator \tilde{S} is the divergence. To compute this, we use a finite difference method to match the method used to discretize the PDE. We use the standard second-order accurate centered difference for the derivatives.

Next, we need the unit normal vectors to the immersed boundary. These can be treated as an input to the method, or we can approximate them if they are unavailable. Approximating the curve with linear elements and using the resulting normal vectors is sufficient for maintaining first-order accuracy. For instance, for an interior domain and a counterclockwise curve parametrization, we can use

$$\mathbf{n}(s_i) = \left[\begin{array}{c} Y(s_{i+1}) - Y(s_{i-1}) \\ -(X(s_{i+1}) - X(s_{i-1})) \end{array} \right] \bigg/ \|\mathbf{X}(s_{i+1}) - \mathbf{X}(s_{i-1})\|_2. \quad (56)$$

For an exterior domain, we would negate this.

Next, we look at the spread operator, $S : \Gamma \rightarrow \mathcal{C}$, which is defined as

$$(SF)(\mathbf{x}) = \int_{\Gamma} F(s) \delta_h(\mathbf{x} - \mathbf{X}(s)) ds. \quad (57)$$

Here, we use the traditional Peskin four-point delta function for δ_h [2], given by

$$\delta_h = \frac{1}{h^2} \phi\left(\frac{x}{h}\right) \phi\left(\frac{y}{h}\right), \quad (58)$$

for $h = \Delta x = \Delta y$ and

$$\phi(r) = \begin{cases} \frac{1}{8}(3 - 2|r| + \sqrt{1 + 4|r| - 4|r|^2}) & 0 \leq |r| \leq 1 \\ \frac{1}{8}(5 - 2|r| - \sqrt{-7 + 12|r| - 4|r|^2}) & 1 \leq |r| \leq 2 \\ 0 & |r| \geq 2 \end{cases}. \quad (59)$$

Then, as mentioned in Section 4.1, we discretize the integral in Equation (57) with respect to arclength, so henceforth, we will treat s as an arclength parameter. With this new assumption on the coordinate s , Δs_i gives the length of the curve connecting the immersed boundary points, $\mathbf{X}(s_i)$ and $\mathbf{X}(s_{i+1})$. Then, the discrete spread operator is given by

$$(SF)(\mathbf{x}) = \sum_{i=1}^{N_{IB}} F(s_i) \delta_h(\mathbf{x} - \mathbf{X}(s_i)) \Delta s_i. \quad (60)$$

Depending on the parametrization, the boundary points may not be equally spaced, but since we will be looking at a periodic distribution on Γ , choosing equally spaced points will give higher accuracy in our integral approximation. In this case, we will space the boundary points so that $\Delta s \approx c\Delta x$ for various c values, and then $\Delta s = L_{IB}/N_{IB}$, where L_{IB} gives the length of the immersed boundary. If the exact values of Δs_i are unavailable, approximations can be made. Again, using $\Delta s_i \approx \|\mathbf{X}(s_{i+1}) - \mathbf{X}(s_i)\|_2$ is sufficient to maintain first-order accuracy.

Lastly, the interpolation operator, $S^* : \mathcal{C} \rightarrow \Gamma$, is similarly discretized as follows.

$$(S^*u)(s) = \int_{\mathcal{C}} u(\mathbf{x}) \delta_h(\mathbf{x} - \mathbf{X}(s)) d\mathbf{x} \approx \sum_i u(\mathbf{x}_i) \delta_h(\mathbf{x}_i - \mathbf{X}(s)) (\Delta x)(\Delta y), \quad (61)$$

where, for a fixed s and a four-point delta function, the sum over the grid points has at most 16 non-zero terms.

5.3. Solution to discrete system for invertible \mathcal{L}

We now describe the method for solving the discretized system

$$\mathcal{L}u + \tilde{S}Q = \tilde{g} \quad \text{in } \mathcal{C} \quad (62a)$$

$$S^*u + \frac{1}{2}Q = U_b \quad \text{on } \Gamma. \quad (62b)$$

In the case that the differential operator is invertible, such as for $\mathcal{L} = \Delta - k^2$, for $k \neq 0$, we can invert the operator to obtain

$$u = -\mathcal{L}^{-1}\tilde{S}Q + \mathcal{L}^{-1}\tilde{g}. \quad (63)$$

Then, by applying the interpolation operator and using Equation (62b), we obtain

$$-(S^*\mathcal{L}^{-1}\tilde{S})Q + \frac{1}{2}Q = U_b - S^*\mathcal{L}^{-1}\tilde{g}. \quad (64)$$

We can therefore solve Equation (62) by first solving Equation (64) for Q and then obtaining u from Equation (62a). Here, the operator that must be inverted,

$-(S^* \mathcal{L}^{-1} \tilde{S}) + \frac{1}{2} \mathbb{I}$, is not symmetric, and we therefore solve for Q with `gmres`², to a tolerance of 10^{-8} , unless otherwise specified.

5.4. Solution to discrete system for Poisson equation

In the case that the differential operator is the periodic Laplacian, $\mathcal{L} = \Delta$, the solution method outlined in the previous section must be adjusted, both for the nullspace of the discrete constraint system and the nullspace of \mathcal{L} .

The boundary value problem given by

$$\Delta u = g \quad \text{in } \Omega \quad (65a)$$

$$u = U_b \quad \text{on } \Gamma \quad (65b)$$

has a unique solution in Ω , but, by using the IB framework, we embed the PDE into a periodic computational domain on which Δ is not invertible, resulting in a nullspace for the differential operator \mathcal{L} . Furthermore, the discretized constraint matrix for the IBDL method also has a nullspace that becomes relevant for large exterior domains. Both issues are discussed in this section.

5.4.1. Nullspace of the constraint system

In the case of the IBSL method applied to the Poisson equation, the matrix

$$\begin{pmatrix} \Delta & S \\ S^* & 0 \end{pmatrix}, \quad (66)$$

is invertible. Therefore, we can use the method presented by Stein et al. [31] to handle the nullspace of the periodic Laplacian and recover the unique solution to the constraint system.

In the case of the IBDL method, however, the matrix

$$\begin{pmatrix} \Delta & \tilde{S} \\ S^* & \frac{1}{2} \mathbb{I} \end{pmatrix}, \quad (67)$$

has a one-dimensional nullspace. The nullspace of the spatially continuous problem is spanned by

$$u = \chi_{C \setminus \Omega} \quad (68a)$$

$$Q = -1, \quad (68b)$$

where $\chi_{C \setminus \Omega}$ gives the indicator function that is 0 on Ω and 1 otherwise. According to Equation (68), since an element of the nullspace would be 0 on the physical

²We utilize `gmres` from MATLAB R2022a [42].

domain, any solution we get would be the same on Ω , and this nullspace would therefore not pose a problem for the IBDL method. However, the discretized problem results in a different *numerical* nullspace. In Section 6.3, we show that for large exterior domains, the IBDL method may not converge to the correct solution. This may be due to the fact that as we increase the domain size, we approach the infinite exterior domain case, for which a double layer potential is unable to represent solutions to the Poisson equation with arbitrary boundary values [51]. As we approach this case, the IBDL method becomes more sensitive to the numerical nullspace.

To solve this issue for large exterior domains, we may use a *completed* double layer representation. There are multiple ways to formulate such a representation for integral equations [37, 52], but we have chosen the method presented by Hsiao and Kress [53] and Hebekker [54] since it easily translates to an IB framework. We therefore formulate the completed representation by the addition of a single layer potential whose strength is a constant multiple of the strength of the double layer potential. The completed system is then given by

$$\Delta u + \eta S Q + \tilde{S} Q = \tilde{g} \quad \text{in } \mathcal{C} \quad (69a)$$

$$S^* u + \frac{1}{2} Q = U_b \quad \text{on } \Gamma, \quad (69b)$$

where η is a positive constant. We will refer to this form of the IBDL method as the *completed IBDL method*. In this case, the matrix

$$\begin{pmatrix} \Delta & \tilde{S} + \eta S \\ S^* & \frac{1}{2} \mathbb{I} \end{pmatrix}, \quad (70)$$

is invertible, and then we need only deal with the nullspace of the periodic Laplacian.

5.4.2. Nullspace of \mathcal{L}

As previously mentioned, the original boundary value problem on Ω has a unique solution, but, by using the IB framework, we embed the PDE into a periodic computational domain on which Δ is not invertible.

We can recover the unique solution to the PDE by a method similar to that presented by Stein et al. [31]. In this process, we first decompose the solution u into

$$u = u_0 + \bar{u}, \quad (71)$$

where u_0 has mean 0 on \mathcal{C} and \bar{u} gives the mean value of u on \mathcal{C} . Then, we use the PDE resulting from either the IBDL or the completed IBDL formulation to derive a solvability condition, resulting in either a condition on g_e or in the addition of another equation to the discrete IBDL system. Details for this process are given in [Appendix C](#).

5.5. Near-boundary points

The replacement of solution values for grid points within m_1 meshwidths of Γ is done with a linear interpolation. For the Dirichlet problem, the interpolation for an individual grid point uses one approximate solution value located about m_2 meshwidths away from Γ and one value approximated from the known solution values located on Γ . For the Neumann problem, the solution values located on Γ are not known, and therefore they are also approximate. Details for this interpolation are given in [Appendix A](#).

In order to complete this step and to isolate the solution on the problem domain, it is necessary to identify grid points as interior or exterior to Γ . Depending on the boundary shape, this can be done with the exact parametrization of the curve, but we can also use a portion of the IBDL method itself to identify grid points interior to the *discretized* curve. Details for this are given in [Appendix D](#).

6. Numerical results

In this section, we apply the Immersed Boundary Double Layer method and discuss numerical results and observations. In [Section 6.1](#), we apply the IBDL method to a Dirichlet Helmholtz problem and demonstrate the efficiency of the method and the convergence of the solution. In [Section 6.2](#), we discuss interpolation widths and other factors affecting the max norm convergence. In [Section 6.3](#), we explore the completed IBDL method for the Dirichlet Poisson problem on a periodic domain. In [Section 6.4](#), we demonstrate the use of the IBDL method on a non-convex exterior domain. In [Section 6.5](#), we explore the convergence of the potential strength Q , and in [Section 6.6](#), we solve a Neumann Helmholtz problem.

6.1. Dirichlet Helmholtz on interior circular domain

First, we look at the PDE

$$\Delta u - u = 0 \quad \text{in } \Omega \tag{72a}$$

$$u = \sin 2\theta \quad \text{on } \Gamma, \tag{72b}$$

where Ω is the interior of a circle of radius 0.25, centered at the origin. The analytic solution is given by

$$u = \frac{I_2(r) \sin 2\theta}{I_2(0.25)}, \tag{73}$$

where I_2 is the first-kind modified Bessel function of order 2. Our computational domain here is the periodic box $[-0.5, 0.5]^2$. We use equally spaced boundary points with $\Delta s \approx c\Delta x$ for various values of c , and the solutions are computed for grid sizes ranging from $N = 2^6$ to 2^{12} .

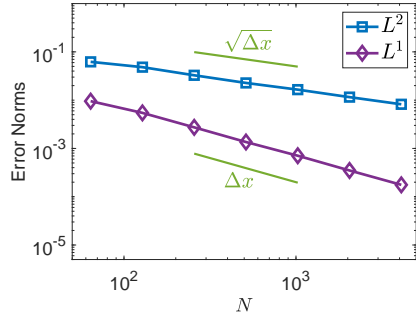
Iteration Counts - Circular Boundary								
Δx	$\Delta s \approx 2\Delta x$		$\Delta s \approx 1.5\Delta x$		$\Delta s \approx 1\Delta x$		$\Delta s \approx 0.75\Delta x$	
	IBSL	IBDL	IBSL	IBDL	IBSL	IBDL	IBSL	IBDL
2^{-6}	17	4	45	5	249	5	491	4
2^{-7}	36	5	57	4	691	5	752	4
2^{-8}	49	5	71	4	1233	4	3057	4
2^{-9}	61	4	110	4	1922	4	5829	4
2^{-10}	68	4	144	4	1936	4	8084	4
2^{-11}	95	4	234	4	4364	4	9335	4
2^{-12}	142	4	303	4	4535	4	10589	4

Table 1: Number of iterations of `minres` and `gmres`, with tolerance 10^{-8} , for the IBSL and IBDL methods, respectively, to solve Equation (72) on the periodic computational domain $[-0.5, 0.5]^2$, where the circular boundary of radius 0.25 has prescribed boundary values given by $U_b = \sin 2\theta$.

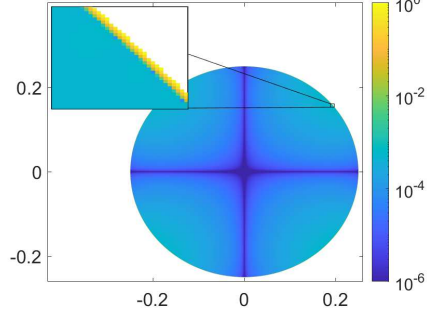
6.1.1. Iteration counts and point spacing

Table 1 gives the iteration counts for the Krylov methods used to solve Equation (72) for the IBSL and IBDL methods. This table illustrates the drastic improvement in efficiency that is a key advantage of the IBDL method. We see that only a small number of iterations are needed to solve for the strength of the IBDL potential. Moreover, the number of iterations remains essentially constant as we refine the mesh or tighten the boundary points relative to the grid. The IBSL method, on the other hand, requires many more iterations, and this iteration count is greatly affected by the mesh size and the boundary point spacing, as previously illustrated in Figure 2b. Tighter boundary points can result in lower quadrature error, while more widely spaced points allow for smoother force distributions and better conditioning in the case of the IBSL method [20]. Making the IBSL method practical therefore often entails special handling, such as using more widely spaced points for discretization of the boundary, while using a denser set of points for the direct Eulerian-Lagrangian interaction [32]. Moreover, to make the IBSL method efficient, one must use a preconditioner [29, 20, 30, 31]. On the other hand, the fact that the IBDL method presented here can be efficiently utilized for both coarsely and finely spaced boundary points means no such step is required for this method.

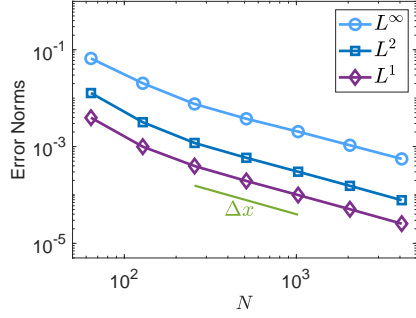
In addition, the iteration counts for the IBSL method are affected by the tolerance for the Krylov method. For example, for $\Delta s \approx 2\Delta x$ and $\Delta x = 2^{-12}$, decreasing the tolerance from 10^{-8} to 10^{-10} increases the iteration count by more than fifty percent, from 142 to 233. For $\Delta s \approx 0.75\Delta x$, the Krylov method cannot reach a tolerance of 10^{-10} for the IBSL method. For the IBDL method, on the other hand, the Krylov method reaches this smaller tolerance in only 5 iterations for either of these cases.



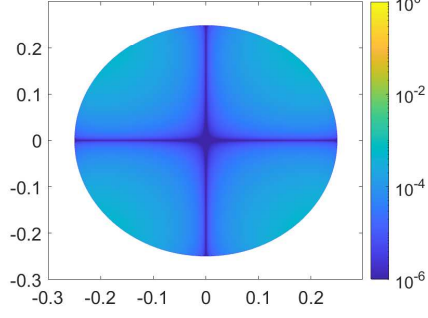
(a) IBDL Refinement, no interpolation



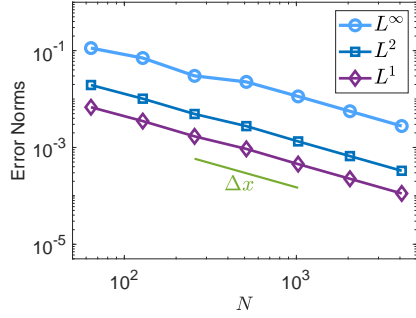
(b) IBDL Refinement, no interpolation



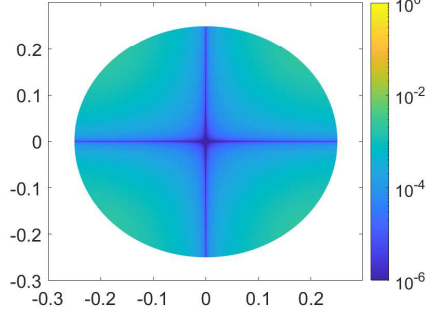
(c) IBDL Refinement



(d) IBDL Error



(e) IBSL Refinement



(f) IBSL Error

Figure 5: Refinement studies and error plot for solutions to Equation (72) found using the IBSL and IBDL methods. The computational domain is the periodic box $[-0.5, 0.5]^2$, Ω is the interior of a circle of radius 0.25, and the prescribed boundary values are given by $U_b = \sin 2\theta$. Figures 5a-5b give the plots for the IBDL method, with no interpolation step. Figures 5c-5d are for the IBDL method with an interpolation step, replacing solution values within $m_1 = 6$ meshwidths from the boundary using an interior interpolation point $m_2 = 8$ meshwidths away from the boundary. Figures 5e-5f are for the IBSL method. The error plots are shown for the grid spacing $\Delta x = 2^{-12}$. All methods use boundary point spacing of $\Delta s \approx 0.75\Delta x$.

6.1.2. Accuracy

To illustrate that the IBDL gives first-order convergence away from the boundary by a distance that is $\mathcal{O}(\Delta x)$, Figure 5a shows the L^1 and L^2 refinement studies for the IBDL solution to Equation (72), obtained without the interpolation step. We observe $\mathcal{O}(\Delta x)$ convergence for L^1 and $\mathcal{O}(\sqrt{\Delta x})$ convergence for L^2 . This indicates that we get first-order pointwise convergence in the solution away from the boundary. This is also illustrated in Figure 5b, where the large errors are seen only within a few meshwidths of the boundary. Therefore, as previously discussed, the interpolation step is not necessary unless we wish to recover pointwise convergence in this small region near the boundary, which is $\mathcal{O}(\Delta x)$ in width.

We then implement the IBDL method, including the interpolation step, in which we replace solution values within $m_1 = 6$ meshwidths of the boundary and use interpolation points located $m_2 = 8$ meshwidths from the boundary. Figures 5e-5c compare the IBSL and IBDL refinement studies, and we see that with the interpolation step, we maintain first-order convergence of the solution on the entire PDE domain. Figures 5f-5d illustrate the solution errors for the two methods, and the errors from the IBDL method are actually lower for this problem. In general, the two methods typically give errors of comparable size.

6.2. Interpolation width and pointwise convergence

As was discussed in Section 4.2, the discontinuity in the solution across the boundary prevents the method from achieving first-order convergence in the max norm near the boundary. As seen in Figure 4, the largest errors are confined to a region of about 2-3 meshwidths due to the support of the discrete delta function. However, there is also a wider region to which the numerical method spreads the errors. The physical length of the region on which the pointwise error fails to converge approaches 0 as the grid is refined, so if we only need the solution away from the boundary, we can proceed with the method as illustrated, or even omit the interpolation step altogether. However, in this section, we will examine this issue more closely and investigate choices that can be made to recover pointwise convergence for the entire PDE domain.

6.2.1. Finite difference vs. Fourier spectral discretization

We found that one key factor affecting the spread of error is the numerical method used to discretize the PDE operator. We therefore start by revisiting Equation (72) and utilizing both finite difference and Fourier spectral methods for discretization. We extend our refinement study to an even finer mesh of $N = 2^{14}$ and explore different values for m_1 , the number of meshwidths from the boundary for which interpolation is used. For all of these, we use an interior interpolation point that is $m_2 = m_1 + 2$ meshwidths from the boundary. Figure 6 shows the corresponding L^∞ refinement studies. In Figure 6a, we can see that

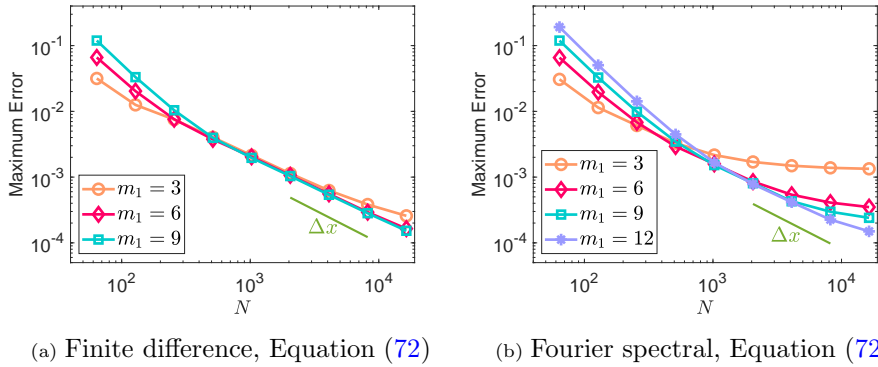


Figure 6: The L^∞ refinement studies for solving Equation (72) with the IBDL method. The computational domain is the periodic box $[-0.5, 0.5]^2$, Ω is the interior of a circle of radius 0.25, the boundary point spacing is $\Delta s \approx 0.75\Delta x$, and m_1 is varied. Figure 6a is found using a finite difference method for discretization of the PDE, and Figure 6b is found using a Fourier spectral method.

$m_1 = 6$ is sufficient to maintain first-order pointwise convergence when using a finite difference discretization. Using a Fourier spectral method, on the other hand, requires a larger value of m_1 . For low, fixed values of m_1 , we see that once the error is small enough, the Fourier spectral method gives a diminishing rate of pointwise convergence and eventually a failure to converge.

To further explore this phenomenon, we next look at the PDE

$$\Delta u - u = -(x + y) \quad \text{in } \Omega \quad (74a)$$

$$u = x + y \quad \text{on } \Gamma, \quad (74b)$$

where Ω is the interior of a circle of radius 0.25, centered at the origin. The analytic solution is given by $u = x + y$. Figures 7a-7b show the L^∞ refinement studies for this problem. Due to the linearity of the solution, the primary source of error is the discontinuity, and this allows us to observe the aforementioned behavior on coarser grids. We can see that the lack of convergence with the Fourier spectral method is worse for this problem, but we see that $m_1 = 6$ is still sufficient to maintain convergence using a finite difference method.

To explore this phenomenon a little more closely, we also omit the interpolation step of the method and examine cross-sections of the error, located at $y = 0$, for which the boundary point is located at $x = -0.25$. Figures 7c-7d show these error cross-sections on a relatively coarse grid of $N = 2^8$ and a fine grid of $N = 2^{14}$. Each marker on the plot represents a grid point on the mesh. For the coarse grid, we see in Figure 7c that the pointwise errors for both methods decrease to the size of the interior error within a couple meshwidths. For the fine grid, however, the Fourier spectral method takes more meshwidths to decrease to the level of the interior error than the finite difference method.

This illustrates the further spreading out of the error that takes place when using the Fourier spectral method due to the slow convergence of errors in a truncated Fourier series for a discontinuity. It is important to note, however, that while the number of meshwidths affected increases as the grid is refined, the physical distance affected still decreases. This is clear when observing the different scaling on the x -axes.

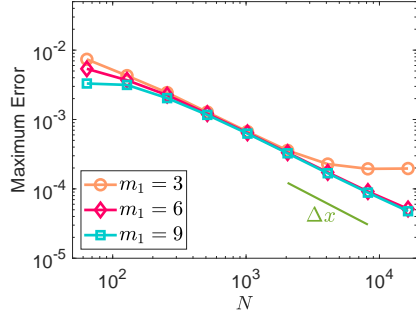
In order to recover pointwise convergence when utilizing a Fourier spectral method, we can choose a function for m_1 that increases as the mesh is refined. We have found that increasing logarithmically seems sufficient for these problems. For example, we could simply increase m_1 by 2 each time the number of grid points, N , is doubled. By doing this, we use interpolation at a greater number of meshwidths as we refine the grid, but, again, the physical distance on which we use interpolation is still decreasing relatively quickly towards 0. Figures 8a and 8b illustrate using such a function for m_1 for Equations (72) and (74), respectively. The function we use is $m_1 = 2(\log_2 N - 4)$, which gives m_1 values ranging from 4 to 20 on these grid sizes. We see that this option recovers pointwise convergence.

6.2.2. Boundary point spacing

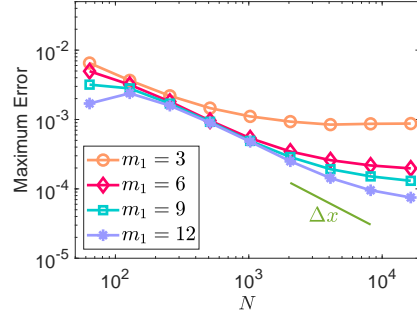
In addition to the PDE discretization and interpolation width, one other factor affecting the error spread is the boundary point spacing. We have observed that in general, using tightly spaced boundary points gives better pointwise convergence for a fixed interpolation width, especially in the case of the finite difference method. Specifically, we have seen that keeping $\Delta s \leq 0.75\Delta x$ will help to avoid a slowing pointwise convergence rate. This is illustrated in Figure 9a, which gives the L^∞ refinement studies for Equation (74) using a finite difference discretization, $m_1 = 6$, and various the boundary point spacings. A conventional choice for IB methods is to choose $\Delta s \approx 0.5\Delta x$ in order to avoid fluid leakage through the immersed boundary [2]. This constraint is typically considered to be less important for rigid structures since the boundary points do not move relative to each other; therefore those utilizing an IBSL-like method typically choose $\Delta s \approx \Delta x$ or $\Delta s \approx 2\Delta x$ to control conditioning [19, 20]. However, in the IBDL method, since we saw in Section 6.1 that the iteration count remains essentially unchanged by tightening the boundary points, there is no numerical drawback to using this tighter point spacing.

If we do want to use more widely spaced points, we can simply increase the interpolation widths from the previous section. Figure 9b shows the L^∞ refinement studies for Equation (74) when the boundary point spacing is given by $\Delta s \approx 2\Delta x$ and the interpolation width is varied. In this case of more widely spaced boundary points, increasing m_1 logarithmically as the mesh is refined again recovers pointwise convergence.

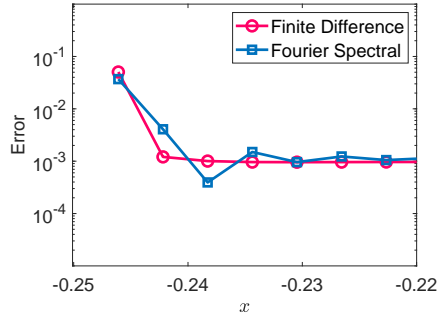
In accordance with the observations seen in Section 6.2, for the majority of this paper, we have elected to use a finite difference PDE discretization, a



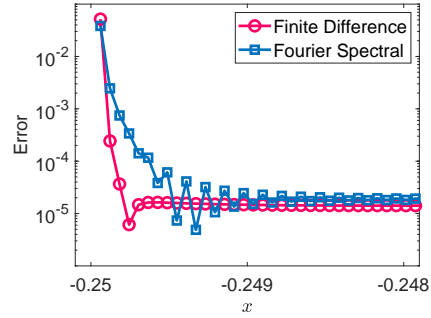
(a) Finite difference, Equation (74)



(b) Fourier spectral, Equation (74)



(c) Pointwise errors on coarse grid



(d) Pointwise errors on fine grid

Figure 7: Figures 7a-7b give the L^∞ refinement studies for solving Equation (74) with the IBDL method for varying values of m_1 . The computational domain is the periodic box $[-0.5, 0.5]^2$, Ω is the interior of a circle of radius 0.25, and the boundary point spacing is $\Delta s \approx 0.75\Delta x$. Figure 7a is found using a finite difference method for discretization of the PDE, and Figure 7b is found using a Fourier spectral method. Figures 7c-7d show the errors along the line $y = 0$ when solving Equation (74) with the IBDL method with no interpolation and using both finite difference and Fourier spectral methods for discretization of the PDE. Figure 7c uses $N = 2^8$, and Figure 7d uses $N = 2^{14}$. Each plot marker represents a grid point on the corresponding mesh.

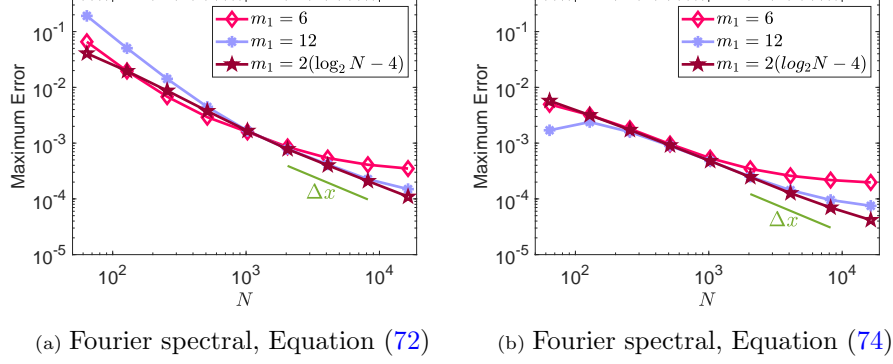


Figure 8: The L^∞ refinement studies for solving Equation (74) using a Fourier spectral method for discretization of the PDE. The value of m_1 is again varied, but also included is an increasing function for m_1 given by $m_1 = 2(\log_2(N) - 4)$.

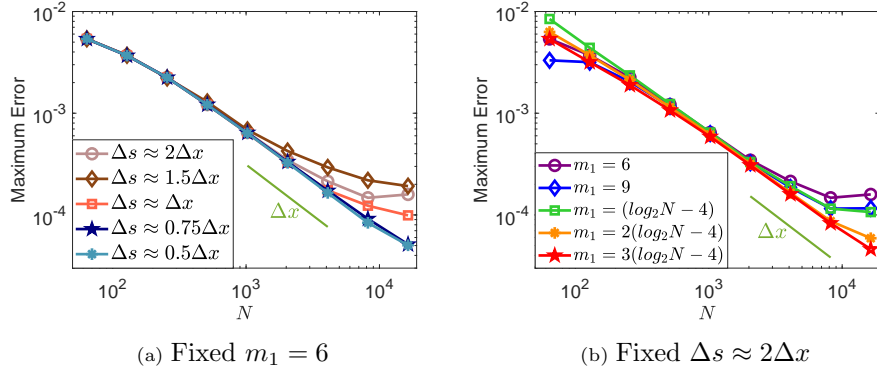


Figure 9: The L^∞ refinement studies for solving Equation (74) with the IBDL method using a finite difference discretization of the PDE. Figure 9a uses a fixed interpolation width of $m_1 = 6$ meshwidths and a second interpolation point $m_2 = 8$ meshwidths from the boundary, and the boundary point spacing is varied. Figure 9b has a wide boundary point spacing of $\Delta s \approx 2\Delta x$, and the interpolation width m_1 is varied.

boundary point spacing of $\Delta s \approx 0.75\Delta x$, and an interpolation width of $m_1 = 6$ meshwidths. Similar results can be found by using a Fourier spectral method, a boundary point spacing of $\Delta s \approx 0.75\Delta x$, and an interpolation width given by $m_1 = 2(\log_2(N) - 4)$. We reiterate that using these options is not essential if we are only concerned with the solution away from the boundary because the width of the region on which the error does not converge pointwise does approach 0 as the grid is refined.

6.3. Poisson equation and completed IBDL method

In this section, we demonstrate the use of the completed IBDL method for large exterior domains, formulated in Section 5.4. To do this, we examine the PDE

$$\Delta u = 4\pi^2 e^{\sin(2\pi x)} \left(\cos^2(2\pi x) - \sin(2\pi x) \right) \quad \text{in } \Omega \quad (75a)$$

$$u = e^{\sin(2\pi x)} \quad \text{on } \Gamma, \quad (75b)$$

for which the analytical solution is given by $u = e^{\sin(2\pi x)}$. We take the PDE domain Ω to be the region in the periodic box $[-L/2, L/2]^2$ that is exterior to a circle of radius 0.25, centered at the origin. We look at both $L = 1$ and $L = 8$. We use finite differences and interpolate values within $m_1 = 6$ meshwidths of the boundary. We first solve these problems using the IBDL method described in Equation (30), without the addition of the single layer potential. Figure 10a illustrates that on the small periodic domain of length 1, the computed solution has first-order convergence. However, Figure 10b demonstrates that for a larger periodic domain of length 8, the IBDL method is unable to achieve convergence to the analytical solution to Equation (75). We next apply the completed IBDL method, described in Equation (69), with $\eta = 10$ for this large computational domain. Figure 10c illustrates we get first order convergence with the completed method.

6.4. Non-convex boundary

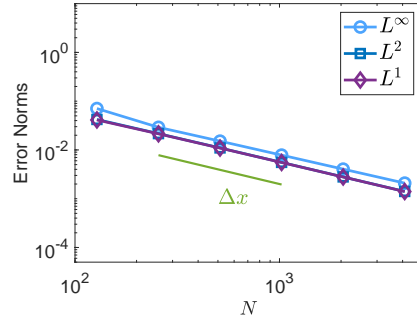
In this section, we demonstrate the effectiveness of the IBDL method for a non-convex boundary. To do this, we use the original IBDL method, without the completion, to solve the PDE

$$\Delta u = \frac{\pi^2}{4} \left(\cos\left(\frac{\pi y}{2}\right) - \sin\left(\frac{\pi x}{2}\right) \right) \quad \text{in } \Omega \quad (76a)$$

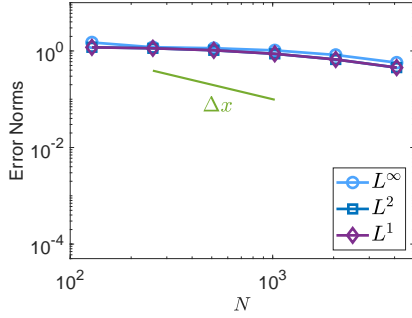
$$u = \sin\left(\frac{\pi x}{2}\right) - \cos\left(\frac{\pi y}{2}\right) \quad \text{on } \Gamma, \quad (76b)$$

where Ω is the region inside the periodic box $[-2, 2]^2$ that is exterior to the ‘starfish’ shape used in [47], which is given by

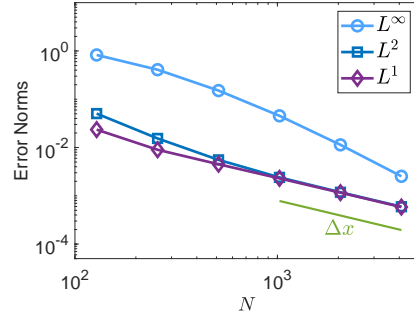
$$\begin{pmatrix} x(\theta) \\ y(\theta) \end{pmatrix} = \left(1 + \frac{\sin(10\pi\theta)}{4} \right) \begin{pmatrix} \cos(2\pi\theta) \\ \sin(2\pi\theta) \end{pmatrix}, \quad (77)$$



(a) IBDL, $L = 1$



(b) IBDL, $L = 8$



(c) Completed IBDL, $L = 8$

Figure 10: Refinement studies for solutions to Equation (75) found using the IBDL method, with finite differences. For Figure 10a, the computational domain is the periodic box $[-0.5, 0.5]^2$, and for Figures 10b-10c, the computational domain is the periodic box $[-4, 4]^2$. Figures 10a-10b use the original IBDL method, and Figure 10c uses the completed IBDL method. Ω is the region in the computational domain exterior to a circle of radius 0.25, centered at the origin. A boundary point spacing of $\Delta s \approx 0.75\Delta x$ is used, and solution values within $m_1 = 6$ meshwidths from the boundary are replaced using a second interpolation point $m_2 = 8$ meshwidths away from the boundary. All errors reported are absolute errors.

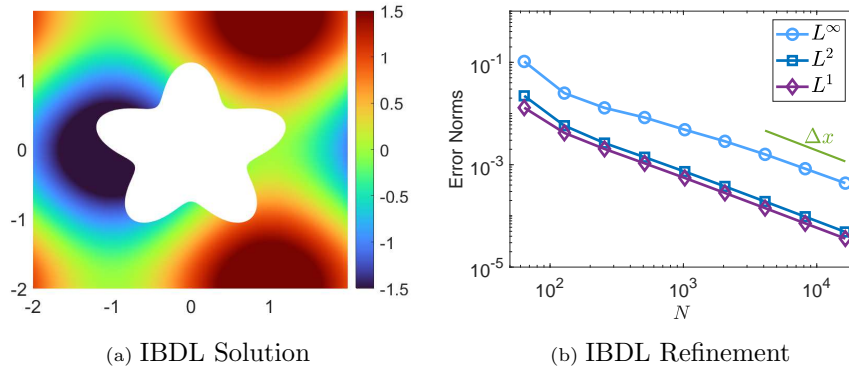


Figure 11: A solution plot and refinement study for solving Equation (76) with the IBDL method. The computational domain is the periodic box $[-2, 2]^2$, Ω is the region exterior to a “starfish” shape, and the prescribed boundary values are given by $U_b = \sin(\pi x/2) - \cos(\pi y/2)$. A boundary point spacing of $\Delta s \approx 0.75\Delta x$ is used, and solution values within $m_1 = 6$ meshwidths from the boundary are replaced using a second interpolation point $m_2 = 8$ meshwidths away from the boundary.

for $0 \leq \theta \leq 1$. We use equally spaced boundary points, with $\Delta s \approx 0.75\Delta x$, and the solutions are computed for grid sizes ranging from $N = 2^6$ to 2^{14} . The analytic solution is given by $u = \sin(\pi x/2) - \cos(\pi y/2)$. For this problem, the IBDL method only requires 13–14 iterations of `gmres`. Figure 11a shows a plot of the solution obtained from the IBDL method, and Figure 11b demonstrates the first-order convergence in the refinement study.

6.5. Convergence of potential strength

In addition to the increased speed with which we solve the system for the potential strength, Q , another benefit of the better conditioning of the IBDL method is that we are more easily able to get convergence in this potential strength. It is a well-known problem that the poor conditioning of the Schur complement results in a noisy force distribution in the IBSL method [55], and this noise is larger for tighter boundary point spacing. Here, we illustrate that in the IBDL method, we obtain much smoother distributions with little need for filtering.

To demonstrate this, we compute the IBSL and IBDL force distributions, F and Q , obtained by solving the interior problem from Section 6.1, where the computational domain is instead the periodic box $[-10, 10]^2$. For estimating convergence, we approximate the exact distributions using a boundary element method, and this larger computational domain allows us to approximate the periodic Green’s function with the free-space Green’s function.

In Figures 12a-12d, for which we use $\Delta s \approx \Delta x$, we see approximately first-order convergence for the IBDL distribution Q and no convergence for the IBSL distribution F . Figure 12a shows that F quickly becomes very noisy as we refine

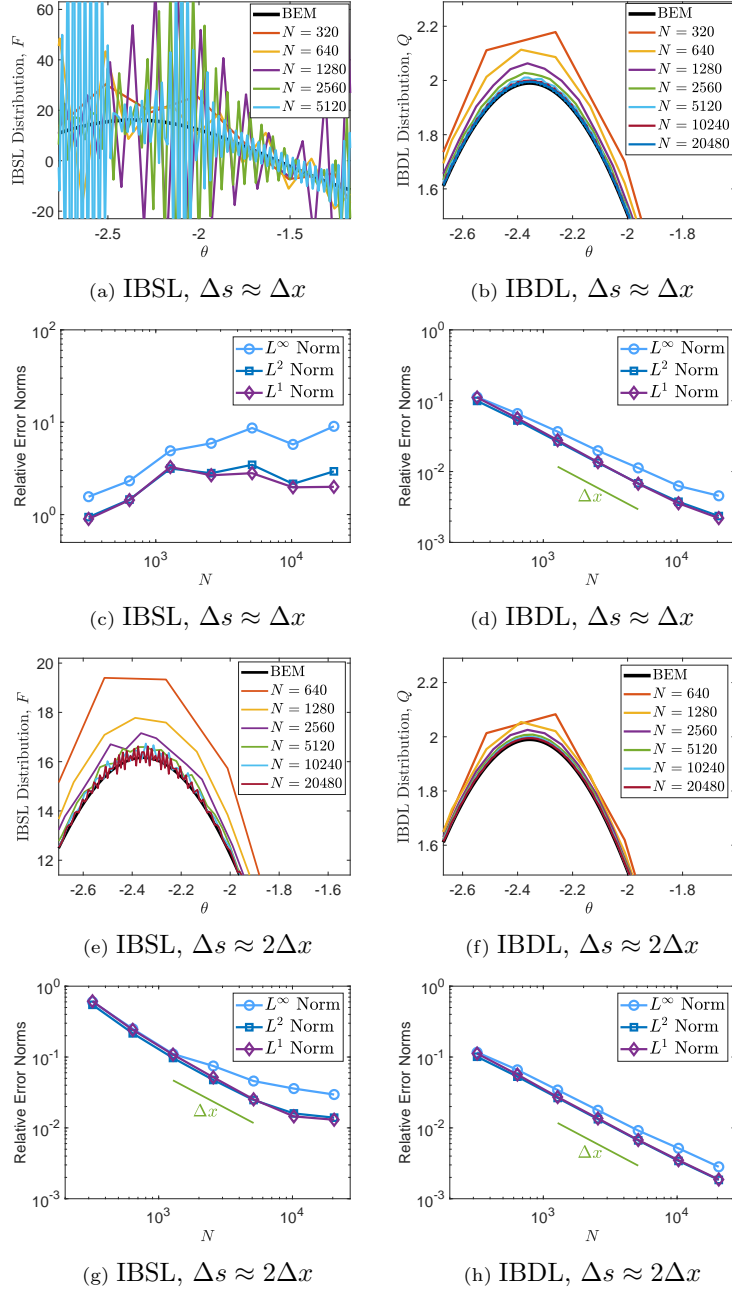


Figure 12: Figures 12a-12b and 12e-12f show portions of the the IBSL and IBDL potential strengths, plotted against the angle θ , for Equation (72). Plots are shown for different mesh sizes, and the boundary point spacing is given by $\Delta s \approx \Delta x$ for Figures 12a-12b and $\Delta s \approx 2\Delta x$ for Figures 12e-12f. The black curves correspond to the distributions found using a boundary element method with uniform, straight line elements and Gauss-Legendre quadrature. These BEM distributions are used to approximate the error, normalized by the maximum value, and Figures 12c-12d and 12g-12h show the corresponding refinement studies.

the grid. As seen in Figure 12b, there is much less noise in Q . Note that the plots only show a portion of the distributions in order to more easily view this noise.

For Figures 12e-12h, we increase the spacing for the boundary points to $\Delta s \approx 2\Delta x$. Then we see some convergence in the IBSL distribution F . However, the IBDL potential strength Q achieves greater convergence and a much lower relative error than F . Therefore, we see that the IBDL method in general allows us to achieve a much more accurate distribution, and the next section demonstrates an application for which this convergence is vital.

6.6. Neumann boundary conditions

As discussed in Section 4.4, we are able to use the connection to integral equations to solve a PDE with Neumann boundary conditions by solving

$$(-S^* \mathcal{L}^{-1} \tilde{S})U_b - \frac{1}{2}U_b = S^* \mathcal{L}^{-1} S V_b - S^* \mathcal{L}^{-1} \tilde{g} \quad (78)$$

for the unknown boundary values U_b . By doing this, we are again inverting an operator corresponding to a second-kind integral operator with a small condition number. Therefore, we are able to get convergence in this boundary distribution, as discussed in the previous section. When we have Neumann boundary conditions, the convergence of the distribution, U_b is especially important because U_b is used when performing our interpolation step for grid points near the boundary. In the Dirichlet case, U_b is known, providing us with more accurate interpolation data, but in the case of Neumann, the values both in the interior and on the boundary are approximate.

We consider the PDE given by

$$\Delta u - u = -(x^2 - y^2) \quad \text{in } \Omega \quad (79a)$$

$$\frac{\partial u}{\partial n} = 8(x^2 - y^2) \quad \text{on } \Gamma, \quad (79b)$$

where Ω is the interior of a circle of radius 0.25, centered at the origin. The analytic solution is given by $u = x^2 - y^2$. Our computational domain here is the periodic box $[-0.5, 0.5]^2$, our boundary point spacing is given by $\Delta s \approx 0.75\Delta x$, and we replace solution values within $m_1 = 6$ meshwidths of the boundary using interior interpolation points located $m_2 = 8$ meshwidths from the boundary. For this problem, our method only requires 4 – 6 iterations of `gmres`. Figure 13 illustrates the refinement studies for the solution values and U_b , and we see approximately first-order convergence in both of these.

7. Discussion

We have developed the Immersed Boundary Double Layer method, a numerical method for linear PDE on complex domains with Dirichlet or Neumann

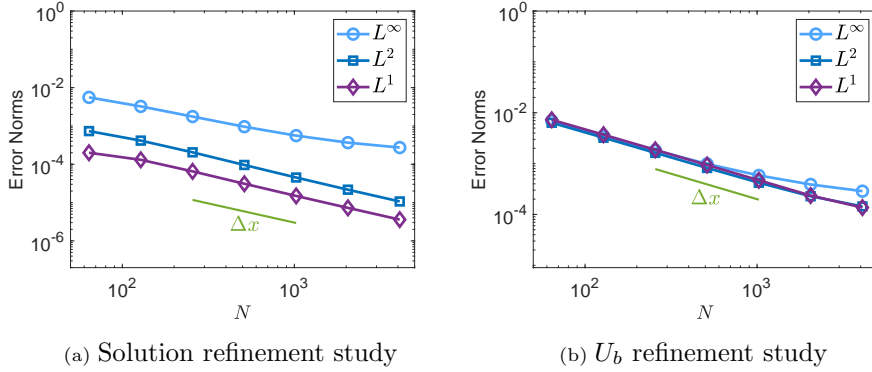


Figure 13: Refinement studies for solving Equation (79) with the method discussed in Section 4.4. The computational domain is the periodic box $[-0.5, 0.5]$, Ω is the interior of a circle of radius 0.25, and the prescribed normal derivatives on the boundary are given by $\partial u / \partial n|_{\Gamma} = 8(x^2 - y^2)$. We use a boundary point spacing of $\Delta s \approx 0.75\Delta x$ and replace solution values within $m_1 = 6$ meshwidths from the boundary using interior interpolation points $m_2 = 8$ meshwidths away from the boundary. Figures 13a and 13b show the refinement studies for the solution errors and the boundary values U_b , respectively.

boundary conditions that is more efficient than the constraint formulation of the Immersed Boundary method. We achieved this greater efficiency by reformulating the IB constraint method to correspond to a regularized double layer integral equation, which has better conditioning than the single layer integral equation to which the constraint formulation corresponds. With this better conditioning, we can solve for the Lagrangian dipole force distribution Q , in a small number of iterations of a Krylov method, and the iteration count does not increase as we refine the mesh. Furthermore, the computed Q is relatively smooth and converges reasonably to the exact potential strength. Both of these are in stark contrast to the IB constraint method, in which the Lagrangian delta force distribution, F , requires many iterations to compute, the number of which increases with finer meshes and tighter boundary point spacing. Additionally, this distribution often fails to converge due to high-frequency noise.

The IBDL method retains much of the flexibility and robustness of the IB method. The communication between the Lagrangian coordinate system and the underlying Cartesian grid is achieved with convolutions with regularized delta functions, and no analytical Green's functions are needed in the computation. Furthermore, minimal geometric information is needed for the immersed boundary. We only need boundary points, unit normals, an indicator function flagging points as inside the PDE domain, Ω , and an indicator function flagging points as near-boundary points. Furthermore, we can reduce this input list to just the set of boundary points. The unit normals can be estimated as described in Section 5.2, and the interior indicator function can be calculated as described in Appendix D. Since such minimal geometric information is needed, this method can be easily used for complex PDE domains. The IBDL method

also maintains flexibility in the PDE discretization, which is a typical advantage of an IB method. In this paper, we have compared two discretizations, and while the width of the interpolation region is affected by the choice, the IBDL method works with either option.

Unlike the IB constraint method, the IBDL method produces a discontinuous solution across the boundary, resulting in a loss of pointwise convergence in a region near the boundary, the width of which approaches 0 as the mesh is refined. If we wish to recover pointwise convergence up to the boundary, we can replace solution values for near-boundary points. In this paper, we have utilized a simple linear interpolation to replace these values. However, there is much work in the realm of boundary integral methods to harness analytical information of the PDE to achieve accurate near-boundary evaluations [46, 47, 36]. The convergence of the potential strength Q opens the door to the possibility of utilizing similar methods in the IBDL context.

The IBDL method is related to the method of immersed layers, presented in the recent work of Eldredge [40]. In this work, Eldredge uses the indicator function discussed in [Appendix D](#) to develop extended forms of PDEs that govern variables that define different functions on either side of the boundary. Jump quantities corresponding to the strengths of single and double layer potentials naturally emerge in the PDEs. The goal of this method is to be able to enforce different constraints on either side of the immersed boundary in order to obtain solutions on both sides and to accurately predict the surface traction on one side of the boundary. With the inclusion of jumps in both the solution and derivative, this method is able to achieve these goals. We should also note here that our application of the IBDL method to a Neumann problem includes a known delta force distribution and was derived from an integral representation containing both single and double layer potentials. Therefore, it can be seen as a specific case of the method of immersed layers [40]. However, if we focus on Dirichlet problems in which the solution is only desired on one side of the immersed boundary, the method of immersed layers again requires inverting an operator corresponding to a first-kind integral equation that is poorly conditioned.

The IBDL method for Dirichlet boundary conditions uses a double layer potential alone, allowing a jump in only the solution values. This allows us to develop a method that corresponds to a second-kind integral equation that can be solved much more efficiently. One can see the IB constraint method of Taira and Colonius [19] as corresponding to a single layer integral representation, the IBDL method presented in this paper as corresponding to a double layer integral representation, and the method of immersed layers of Eldredge [40] as corresponding to an integral representation that includes both single and double layers. And in the case of Dirichlet boundary conditions, the better conditioning of the IBDL operator gives a more efficient method.

We also make note of another difference between the IBDL method and the

method of immersed layers. While [40] uses a lattice Green’s function for unbounded external flows, the IBDL method does not involve an explicit Green’s function. Instead the method obtains the convolution of the boundary potential with a regularized Green’s function by solving the PDE after spreading the boundary potential with the regularized delta function. Thus the IBDL method can be used on more general domains. In this paper we use a periodic computational domain, but we could also easily use other boundary conditions and domains.

Although we focused in this paper on the 2-D Helmholtz and Poisson equations, the method naturally extends to three dimensions and other related equations. The increased efficiency of this method makes it practical for use on time-dependent PDEs. For example, with an implicit time-discretization of the diffusion equation, we could use the IBDL method to solve a Helmholtz equation at each time step. We can also use the IBDL method for a PDE with a nonlinearity by using an implicit-explicit time-stepping scheme, as is done for the IBSE method in Stein et al. [31].

In this paper, we have introduced the IBDL methodology through its application to the Helmholtz and Poisson equations, as a first step towards applying the method to fluid problems involving rigid bodies. Formulating the IBDL method for Stokes and Navier-Stokes equations introduces nontrivial challenges. First, an arbitrary external flow cannot be represented by a double layer potential alone [56]. However, the completed IBDL method required for large exterior domains for the periodic Poisson equation in this work will be utilized to overcome this obstacle. Second, the incompressibility condition introduces challenges for spatial discretization. We have obtained preliminary results applying the IBDL method to Stokes and Navier-Stokes equations, and this work will be presented in a forthcoming paper.

Acknowledgment

This work was supported in part by NSF grant DMS-1664679 to R.D.G.

Appendix A. Interpolation for solution values near the boundary

In this section, we discuss the details of the linear interpolation used to replace solution values within m_1 meshwidths of the boundary. Figure A.14 illustrates the interpolation for one point, \mathbf{x}_p . Given such a point, we first locate the two nearest boundary points, labeled in the picture as \mathbf{x}_1 and \mathbf{x}_2 . We use a projection to find \mathbf{x}_A , the point on the segment between \mathbf{x}_1 and \mathbf{x}_2 that is closest to \mathbf{x}_p . It is given by

$$\mathbf{x}_A = \mathbf{x}_2 + \frac{(\mathbf{x}_2 - \mathbf{x}_p) \cdot (\mathbf{x}_1 - \mathbf{x}_2)}{\|\mathbf{x}_1 - \mathbf{x}_2\|^2}(\mathbf{x}_1 - \mathbf{x}_2). \quad (\text{A.1})$$

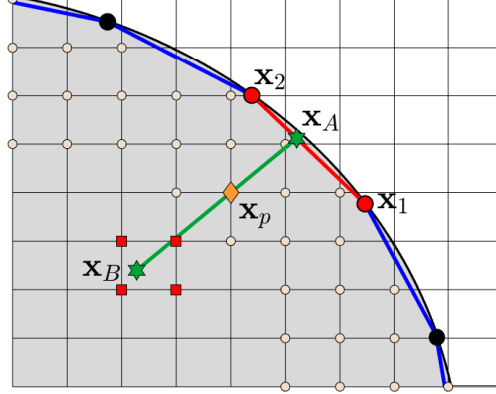


Figure A.14: Illustration of the interpolation step of the IBDL method. The PDE domain Ω is shown in grey. The exact boundary curve is shown in black with black circles indicating immersed boundary points. Lines connecting the IB points are shown in blue. Grid points within $m_1 = 3$ meshwidths of the boundary are indicated by beige circles. The diagram illustrates the process for interpolating the value for one point, denoted with an orange diamond and labeled \mathbf{x}_p . The two closest boundary points are marked with red circles and labeled \mathbf{x}_1 and \mathbf{x}_2 . The closest point on the line segment connecting \mathbf{x}_1 and \mathbf{x}_2 is called \mathbf{x}_A and is marked with a green pentagram. Also marked with a green pentagram is the point $m_2 = 4$ meshwidths away from \mathbf{x}_A , and it is labeled \mathbf{x}_B . These are the two interpolation points for \mathbf{x}_p .

If the curvature and point placements are such that this calculation results in a point not located on the line segment between \mathbf{x}_1 and \mathbf{x}_2 , we simply find the third closest boundary point and use the two outermost points to find \mathbf{x}_A . Next, we use a simple interpolation of the values at \mathbf{x}_1 and \mathbf{x}_2 to approximate the value at \mathbf{x}_A , and this is given by

$$u(\mathbf{x}_A) \approx U_b(\mathbf{x}_1) \frac{\|\mathbf{x}_A - \mathbf{x}_2\|}{\|\mathbf{x}_2 - \mathbf{x}_1\|} + U_b(\mathbf{x}_2) \frac{\|\mathbf{x}_A - \mathbf{x}_1\|}{\|\mathbf{x}_2 - \mathbf{x}_1\|}, \quad (\text{A.2})$$

where the values at \mathbf{x}_1 and \mathbf{x}_2 are denoted with U_b because these are known boundary values.

We next find the second point of interpolation, located m_2 meshwidths away from point \mathbf{x}_A . It is labeled in the figure as \mathbf{x}_B , and it is given by

$$\mathbf{x}_B = \mathbf{x}_A + \frac{\mathbf{x}_p - \mathbf{x}_A}{\|\mathbf{x}_p - \mathbf{x}_A\|} (m_2 \Delta x). \quad (\text{A.3})$$

Note that this step assumes that points are labeled as interior or exterior according to the *discretized* shape created by the IB points. One way of doing this is presented in [Appendix D](#). Otherwise, we would need to verify that \mathbf{x}_B is located on the correct side of the boundary and if not, alter Equation (A.3) to use subtraction instead of addition.

We then estimate the value for \mathbf{x}_B with a bilinear interpolation of the computed solution values at the four grid points located around \mathbf{x}_B , marked in the figure with red squares. Let \mathbf{x}_{00} be the lower left point, \mathbf{x}_{01} be the upper left, and so on, and let d_x and d_y be the x and y distances from \mathbf{x}_B to \mathbf{x}_{00} . Then our bilinear interpolation is

$$\begin{aligned} u(\mathbf{x}_B) \approx & \left(\frac{d_x}{\Delta x}\right)\left(\frac{d_y}{\Delta y}\right)u(\mathbf{x}_{11}) + \left(\frac{d_y}{\Delta y}\right)\left(1 - \frac{d_x}{\Delta x}\right)u(\mathbf{x}_{01}) \\ & + \left(\frac{d_x}{\Delta x}\right)\left(1 - \frac{d_y}{\Delta y}\right)u(\mathbf{x}_{10}) + \left(1 - \frac{d_x}{\Delta x} - \frac{d_y}{\Delta y} + \left(\frac{d_x}{\Delta x}\right)\left(\frac{d_y}{\Delta y}\right)\right)u(\mathbf{x}_{00}) \end{aligned} \quad (\text{A.4})$$

Note that if \mathbf{x}_B is located directly on a gridline, this can be simplified.

Once we have the approximated values at \mathbf{x}_B and \mathbf{x}_A , we again use a simple linear interpolation to approximate $u(\mathbf{x}_p)$, and this is given by

$$u(\mathbf{x}_p) \approx u(\mathbf{x}_A) \frac{\|\mathbf{x}_B - \mathbf{x}_p\|}{\|\mathbf{x}_B - \mathbf{x}_A\|} + u(\mathbf{x}_B) \frac{\|\mathbf{x}_A - \mathbf{x}_p\|}{\|\mathbf{x}_B - \mathbf{x}_A\|}. \quad (\text{A.5})$$

Appendix B. Immersed Boundary formulation of the Neumann Helmholtz problem

As stated in Section 4.4, the IB formulation of the Neumann problem is given by

$$\mathcal{L}u + \tilde{S}U_b + SV_b = g \quad \text{in } \mathcal{C} \quad (\text{B.1a})$$

$$S^*u = \frac{1}{2}U_b \quad \text{on } \Gamma, \quad (\text{B.1b})$$

where $V_n \equiv \partial u / \partial n|_\Gamma$ gives the known normal derivatives on Γ , and U_b gives the unknown distribution of solution values on Γ . V_b corresponds to the strength of a single layer potential and U_b to the strength of a double layer potential.

Starting with Equation (B.1a), we have

$$\mathcal{L}u = -\tilde{S}U_b - SV_b = -\nabla \cdot \int_\Gamma U_b(s) \mathbf{n}(s) \delta_h(\mathbf{x} - \mathbf{X}(s)) ds - \int_\Gamma V_b(s) \delta_h(\mathbf{x} - \mathbf{X}(s)) ds. \quad (\text{B.2})$$

Inverting the operator and using that $\mathcal{L}G_h(\mathbf{x}, \mathbf{x}_0) = -\delta_h(\mathbf{x} - \mathbf{x}_0)$, we get

$$u(\mathbf{x}) = \nabla \cdot \int_\Gamma U_b(s) \mathbf{n}(s) G_h(\mathbf{x}, \mathbf{X}(s)) ds + \int_\Gamma V_b(s) G_h(\mathbf{x}, \mathbf{X}(s)) ds \quad (\text{B.3})$$

for $\mathbf{x} \in \Omega \setminus \Gamma$. Bringing in the divergence and manipulating the expression, we get

$$u(\mathbf{x}) = \int_\Gamma U_b(s) \nabla G_h(\mathbf{x}, \mathbf{X}(s)) \cdot \mathbf{n}(s) ds + \int_\Gamma V_b(s) G_h(\mathbf{x}, \mathbf{X}(s)) ds \quad (\text{B.4})$$

The second equation of the method, Equation (B.1b) gives us

$$\frac{1}{2}U_b(s') = \int_{\mathcal{C}} u(\mathbf{x})\delta_h(\mathbf{x} - \mathbf{X}(s'))dx. \quad (\text{B.5})$$

Combining Equation (B.4) with Equation (B.5), changing the order of integration, and recognizing the presence of $G_{hh} = G_h * \delta_h$, we get

$$\frac{1}{2}U_b(s') = \int_{\Gamma} U_b(s)\nabla G_{hh}(\mathbf{X}(s'), \mathbf{X}(s)) \cdot \mathbf{n}(s)ds + \int_{\Gamma} V_b(s)G_{hh}(\mathbf{X}(s'), \mathbf{X}(s))ds. \quad (\text{B.6})$$

Note that due to the presence of a double layer potential, as discussed in Section 4.1, we assume that $\mathbf{X}(s)$ is the arclength parametrization of Γ so that $|\partial\mathbf{X}(s)/\partial s| = 1$.

The symmetry of the Green's function, which is preserved through convolutions with the regularized delta function, gives us that $G_{hh}(\mathbf{X}(s'), \mathbf{X}(s)) = G_{hh}(\mathbf{X}(s), \mathbf{X}(s'))$. Additionally, the odd symmetry of the gradient of the Green's function gives us $\nabla G_{hh}(\mathbf{X}(s'), \mathbf{X}(s)) = -\nabla G_{hh}(\mathbf{X}(s), \mathbf{X}(s'))$ [34]. Using these to switch the arguments of these functions, we get

$$\frac{1}{2}U_b(s') = - \int_{\Gamma} U_b(s)\nabla G_{hh}(\mathbf{X}(s), \mathbf{X}(s')) \cdot \mathbf{n}(s)ds + \int_{\Gamma} V_b(s)G_{hh}(\mathbf{X}(s), \mathbf{X}(s'))ds. \quad (\text{B.7})$$

Appropriately redefining U_b and V_b as functions of \mathbf{x} , we get

$$\begin{aligned} \frac{1}{2}U_b(\mathbf{X}(s')) &= - \int_{\Gamma} U_b(\mathbf{X}(s))\nabla G_{hh}(\mathbf{X}(s'), \mathbf{X}(s)) \cdot \mathbf{n}(s)ds \\ &\quad + \int_{\Gamma} V_b(\mathbf{X}(s))G_{hh}(\mathbf{X}(s'), \mathbf{X}(s))ds. \end{aligned} \quad (\text{B.8})$$

Recall that the integral equation for \mathbf{X}_0 on the boundary is given by

$$\begin{aligned} u(\mathbf{X}_0) &= \int_{\Gamma}^{PV} \nabla u(\mathbf{x}) \cdot \mathbf{n}(\mathbf{x})G(\mathbf{x}, \mathbf{X}_0)dl(\mathbf{x}) \\ &\quad - \int_{\Gamma} u(\mathbf{x})\nabla G(\mathbf{x}, \mathbf{X}_0) \cdot \mathbf{n}(\mathbf{x})dl(\mathbf{x}) + \frac{1}{2}u(\mathbf{X}_0). \end{aligned} \quad (\text{B.9})$$

Using our arclength parametrization and combining the $u(\mathbf{X}_0)$ terms, we can rewrite this as

$$\begin{aligned} \frac{1}{2}u(\mathbf{X}(s')) &= - \int_{\Gamma}^{PV} u(\mathbf{X}(s))\nabla G(\mathbf{X}(s), \mathbf{X}(s')) \cdot \mathbf{n}(\mathbf{X}(s))ds \\ &\quad + \int_{\Gamma} G(\mathbf{X}(s), \mathbf{X}(s'))\nabla u(\mathbf{X}(s)) \cdot \mathbf{n}(\mathbf{X}(s))ds. \end{aligned} \quad (\text{B.10})$$

By comparing Equations (B.8) and (B.10), we can see that the IB formulation presented in Equation (B.1) is equivalent to a *regularized* integral equation.

Appendix C. Nullspace of periodic Laplacian

In the case that the differential operator is the periodic Laplacian, the original boundary value problem on Ω has a unique solution, but, by using the IB framework, we embed the PDE into a periodic computational domain on which Δ is not invertible. To recover the unique solution to the PDE, we follow a method similar to that presented by Stein et al. [31].

We begin by decomposing the solution u into

$$u = u_0 + \bar{u}, \quad (\text{C.1})$$

where u_0 has mean 0 on \mathcal{C} and \bar{u} gives the mean value of u on \mathcal{C} . The PDE on \mathcal{C} that results from the completed IBDL formulation in Equation (69a) is given by

$$\Delta u_0 + \eta SQ + \nabla \cdot (SQ\mathbf{n}) = \tilde{g}. \quad (\text{C.2})$$

To derive the solvability condition, we integrate Equation (C.2) over a general computational domain \mathcal{C} . Noting that our spread operator is defined using a regularized delta function, the functions are smooth, and we can use the divergence theorem. Let us use $\partial\mathcal{C}$ as the boundary of \mathcal{C} and $\mathbf{n}_{\mathcal{C}}$ as the unit normal on $\partial\mathcal{C}$, to distinguish it from \mathbf{n} , which we continue to use as the unit normal on the immersed boundary Γ . We then get

$$\int_{\partial\mathcal{C}} \nabla u_0 \cdot \mathbf{n}_{\mathcal{C}} dl(\mathbf{x}) + \eta \int_{\mathcal{C}} SQ d\mathbf{x} + \int_{\partial\mathcal{C}} SQ\mathbf{n} \cdot \mathbf{n}_{\mathcal{C}} dl(\mathbf{x}) = \int_{\mathcal{C}} \tilde{g} d\mathbf{x}. \quad (\text{C.3})$$

If Γ is away from $\partial\mathcal{C}$, the third term vanishes due to the compact support of the integrand. Then, if we take \mathcal{C} to be the periodic box used in this work, the first term also disappears. Using that $\int_{\mathcal{C}} SQ d\mathbf{x} = \int_{\Gamma} Q ds$, the solvability condition on the periodic computational domain \mathcal{C} then has the form

$$\eta \int_{\Gamma} Q ds = \int_{\mathcal{C}} \tilde{g}(\mathbf{x}) d\mathbf{x}. \quad (\text{C.4})$$

When we are not using the completed formulation, since $\eta = 0$, we can easily satisfy this condition with our choice of g_e . For example, we can choose

$$g_e(\mathbf{x}) = -\frac{1}{|\mathcal{C} \setminus \Omega|} \int_{\Omega} g(\mathbf{x}) d\mathbf{x}, \quad (\text{C.5})$$

where we use $|\cdot|$ to denote the area of the domain. With this constraint satisfied, the solution to

$$\Delta u + \nabla \cdot (SQ\mathbf{n}) = \tilde{g} \quad (\text{C.6a})$$

$$S^*u + \frac{1}{2}Q = U_b \quad (\text{C.6b})$$

can be found, and it is unique up to an additive constant. Therefore, since we are not interested in the solution on the nonphysical domain, $\mathcal{C} \setminus \Omega$, we can use the solution with mean 0 on \mathcal{C} . As discussed in Section 5.4.1, any other solution would give the same unique solution on the PDE domain Ω .

If, on the other hand, we use the completed IBDL method, we can use the constraint in Equation (C.4) to find the value of \bar{u} . Discretizing the constraint, we can then summarize the discrete IBDL system as

$$\Delta u_0 + \eta S Q + \tilde{S} Q = \tilde{g} \quad (\text{C.7a})$$

$$S^* u_0 + \bar{u} \mathbf{1}_{N_{IB}} + \frac{1}{2} Q = U_b \quad (\text{C.7b})$$

$$\eta(\Delta s) \mathbf{1}_{N_{IB}}^\top Q = (\Delta x \Delta y) \mathbf{1}_{N^2}^\top \tilde{g}, \quad (\text{C.7c})$$

where $\mathbf{1}_{N^2}$ denotes a vector of length N^2 consisting of all ones. With the solvability constraint satisfied, we can then find the unique solution to Equation (C.7). Letting Δ_0^{-1} denote the operation that inverts the Laplacian by returning a solution with mean 0 on \mathcal{C} , we have $\Delta_0^{-1} \Delta u_0 = u_0$. Using this to invert the Laplacian in Equation (C.7a) and then applying S^* , we get

$$S^* u_0 + \eta S^* \Delta_0^{-1} S Q + S^* \Delta_0^{-1} \tilde{S} Q = S^* \Delta_0^{-1} \tilde{g}. \quad (\text{C.8})$$

Then, we can replace $S^* u_0$ using Equation (C.7b), and we get the the following system of discrete equations, for which we use `gmres` to solve for Q and \bar{u} :

$$-(S^* \Delta_0^{-1} \tilde{S}) Q - \eta (S^* \Delta_0^{-1} S) Q + \bar{u} \mathbf{1}_{N_{IB}} + \frac{1}{2} Q = U_b - S^* \Delta_0^{-1} \tilde{g} \quad (\text{C.9a})$$

$$\eta(\Delta s) \mathbf{1}_{N_{IB}}^\top Q = (\Delta x \Delta y) \mathbf{1}_{N^2}^\top \tilde{g} \quad (\text{C.9b})$$

We can then obtain u by computing

$$u = -\Delta_0^{-1} (\tilde{S} + \eta S) Q + \Delta_0^{-1} \tilde{g} + \bar{u} \mathbf{1}_{N^2}. \quad (\text{C.10})$$

Appendix D. Using IBDL method to flag interior grid points

In this section, we show that by using analytical features of the indicator function for the interior of the immersed boundary $f\Gamma$, we arrive at a familiar IBDL expression that enables us to use the framework already set forth in order to flag grid points as either exterior or interior to Γ . It is useful to have the points flagged as such in order to identify the physical domain of the solution, as well as for completing the interpolation step discussed in Appendix A. Eldredge also discusses this in Appendix A.2 of [40], and his work uses such an indicator function as a foundation on which to build PDEs that govern different variables on different sides of the immersed boundary. Here, we present the derivation

and application of this mechanism in the context of the IBDL method and also discuss how to apply it to a periodic computational domain.

Let the indicator function be defined as

$$\chi(\mathbf{x}) = \begin{cases} 1 & \mathbf{x} \text{ in } \Omega \\ 0 & \mathbf{x} \text{ in } \mathcal{C} \setminus \Omega, \end{cases} \quad (\text{D.1})$$

where we assume here that Ω is the interior of Γ . Then, using a test function, ψ , we have

$$\int_{\mathcal{C}} \chi \Delta \psi d\mathbf{x} = \int_{\Omega} \Delta \psi d\mathbf{x} = \int_{\Gamma} \nabla \psi \cdot \mathbf{n} dl(\mathbf{x}), \quad (\text{D.2})$$

where we first use the definition of χ and then the divergence theorem. Then, since the weak derivative of χ is $\nabla \chi$ such that

$$\int_{\mathcal{C}} \nabla \chi \cdot \nabla \psi d\mathbf{x} = - \int_{\mathcal{C}} \chi \Delta \psi d\mathbf{x}, \quad (\text{D.3})$$

we see from the last term in Equation (D.2) that the weak derivative is given by

$$\nabla \chi = -\delta(\mathbf{x} - \mathbf{X})\mathbf{n}(\mathbf{x}), \quad (\text{D.4})$$

where the \mathbf{X} is a point on Γ , indicating that the support of $\nabla \chi$ is Γ .

We therefore see that

$$-\Delta \chi = -\nabla \cdot \nabla \chi = \nabla \cdot (\delta \mathbf{n}). \quad (\text{D.5})$$

We can recognize $\nabla \cdot (\delta \mathbf{n})$ as the continuous version of the term found in the IBDL method, $\tilde{S}Q = \nabla \cdot (SQ\mathbf{n})$, where Q is a constant distribution of 1. This then gives us a way to construct the indicator function χ by solving the PDE on \mathcal{C} given by

$$\Delta u + \tilde{S}\mathbf{n} = 0, \quad (\text{D.6})$$

using the method already in place for the IBDL method.

Then, if we are using a periodic computational domain, as we do in this paper, u is only unique up to an additive constant. Therefore, we can first find the solution with mean 0 on \mathcal{C} , as discussed in [Appendix C](#). Then, to shift the exterior values to 0, we simply need to subtract the appropriate constant, which can be approximated using a value of u far from Γ . A likely choice is the corner of the periodic domain. Subtracting this value from u then results in a regularized indicator function, χ_h , that is approximately equal to 1/2 on the boundary Γ . To retrieve the final indicator function, we simply set all values of χ_h that are less than 1/2 equal to 0 and all those above 1/2 to 1. Then χ is the indicator function described in Equation (D.1) that is equal to 1 for all points on the interior of the discretized boundary Γ .

References

- [1] C. Peskin, Numerical analysis of blood flow in the heart, *Journal of Computational Physics* 25 (1977) 220–252. doi:[10.1016/0021-9991\(77\)90100-0](https://doi.org/10.1016/0021-9991(77)90100-0).
- [2] C. S. Peskin, The immersed boundary method, *Acta Numerica* 11 (2002) 479–517. doi:[10.1017/S0962492902000077](https://doi.org/10.1017/S0962492902000077).
- [3] C. Peskin, Flow patterns around heart valves: A digital computer method for solving the equations of motion, PhD thesis. Albert Einstein Coll. Med. University Microfilms (1972) 378: 72–30.
- [4] C. Peskin, The fluid dynamics of heart valves: experimental, theoretical and computational methods, *Annual Review of Fluid Mechanics* 14 (1981) 235–259. doi:[10.1146/annurev.fl.14.010182.001315](https://doi.org/10.1146/annurev.fl.14.010182.001315).
- [5] D. M. McQueen, C. S. Peskin, E. L. Yellin, Fluid dynamics of the mitral valve: Physiological aspects of a mathematical model, *American Journal of Physiology* 11 (6) (1982) H1095–H1110. doi:[10.1152/ajpheart.1982.242.6.H1095](https://doi.org/10.1152/ajpheart.1982.242.6.H1095).
- [6] D. M. McQueen, C. S. Peskin, A three-dimensional computer model of the human heart for studying cardiac fluid dynamics, *Computer Graphics* 34 (1) (2000) 56–60. doi:[10.1145/563788.604453](https://doi.org/10.1145/563788.604453).
- [7] B. E. Griffith, D. M. McQueen, C. S. Peskin, Simulating the fluid dynamics of natural and prosthetic heart valves using the immersed boundary method, *International Journal of Applied Mechanics* 1 (1) (2009) 137–177. doi:[10.1142/S1758825109000113](https://doi.org/10.1142/S1758825109000113).
- [8] C. D. Eggleton, A. S. Popel, Large deformation of red blood cell ghosts in a simple shear flow, *Physics of Fluids* 10 (8) (1998) 1834–1845. doi:[10.1063/1.869703](https://doi.org/10.1063/1.869703).
- [9] A. L. Fogelson, C. S. Peskin, A fast numerical method for solving the three-dimensional Stokes’ equations in the presence of suspended particles, *Journal of Computational Physics* 79 (1988) 50–69. doi:[10.1016/0021-9991\(88\)90003-4](https://doi.org/10.1016/0021-9991(88)90003-4).
- [10] J. M. Stockie, S. I. Green, Simulating the motion of flexible pulp fibres using the immersed boundary method, *Journal of Computational Physics* 147 (1) (1998) 147–165. doi:[10.1006/jcph.1998.6086](https://doi.org/10.1006/jcph.1998.6086).
- [11] Y. Kim, C. S. Peskin, Penalty immersed boundary method for an elastic boundary with mass, *Physics of Fluids* 19 (5) (2007) 1–18. doi:[10.1063/1.2734674](https://doi.org/10.1063/1.2734674).
- [12] J. M. Stockie, Modeling and simulation of porous immersed boundaries, *Computers and Structures* 87 (11) (2009) 701–709. doi:[10.1016/j.compstruc.2008.11.001](https://doi.org/10.1016/j.compstruc.2008.11.001).

- [13] S. Lim, A. Ferent, S. Wang, C. S. Peskin, Dynamics of a closed rod with twist and bend in fluid, *SIAM Journal on Scientific Computing* 31 (1) (2008) 273–302. doi:[10.1137/070699780](https://doi.org/10.1137/070699780).
- [14] S. Olson, S. Lim, R. Cortez, Modeling the dynamics of an elastic rod with intrinsic curvature and twist using a regularized Stokes formulation, *Journal of Computational Physics* 238 (2013) 169–187. doi:[10.1016/j.jcp.2012.12.026](https://doi.org/10.1016/j.jcp.2012.12.026).
- [15] D. C. Bottino, Modeling viscoelastic networks and cell deformation in the context of the immersed boundary method, *Journal of Computational Physics* 147 (1) (1998) 86–113. doi:[10.1006/jcph.1998.6074](https://doi.org/10.1006/jcph.1998.6074).
- [16] W. Strychalski, R. D. Guy, Viscoelastic immersed boundary methods for zero Reynolds number flow, *Communications in Computational Physics* 12 (2) (2012) 462–478. doi:[10.4208/cicp.050211.090811s](https://doi.org/10.4208/cicp.050211.090811s).
- [17] R. Cortez, N. Cowen, L. Fauci, R. Dillion, Simulation of swimming organisms: Coupling internal mechanics with external fluid dynamics, *Computing in Science and Engineering* 6 (3) (2004) 3–45. doi:[10.1109/MCISE.2004.1289307](https://doi.org/10.1109/MCISE.2004.1289307).
- [18] R. H. Dillon, L. J. Fauci, An integrative model of internal axoneme mechanics and external fluid dynamics in ciliary beating, *Journal of Theoretical Biology* 207 (3) (2000) 415–430. doi:[10.1006/jtbi.2000.2182](https://doi.org/10.1006/jtbi.2000.2182).
- [19] K. Taira, T. Colonius, The immersed boundary method: A projection approach, *Journal of Computational Physics* 225 (2007) 2118–2137. doi:[10.1016/j.jcp.2007.03.005](https://doi.org/10.1016/j.jcp.2007.03.005).
- [20] B. Kallemov, A. Bhalla, B. Griffith, A. Donev, An immersed boundary method for rigid bodies, *Communications in Applied Mathematics and Computational Science* 11 (1) (2016) 79–141. doi:[10.2140/camcos.2016.11.79](https://doi.org/10.2140/camcos.2016.11.79).
- [21] A. Bhalla, R. Bale, B. Griffith, N. Patankar, A unified mathematical framework and an adaptive numerical method for fluid-structure interaction with rigid, deforming, and elastic bodies, *Journal of Computational Physics* 250 (2013) 446–476. doi:[10.1016/j.jcp.2013.04.033](https://doi.org/10.1016/j.jcp.2013.04.033).
- [22] M. Uhlmann, An immersed boundary method with direct forcing for the simulation of particulate flows, *Journal of Computational Physics* 209 (2) (2005) 448–476. doi:[10.1016/j.jcp.2005.03.017](https://doi.org/10.1016/j.jcp.2005.03.017).
- [23] S. Su, M. Lai, C. Lin, An immersed boundary technique for simulating complex flows with rigid boundary, *Computers and Fluids* 36 (2007) 313–324. doi:[10.1016/j.compfluid.2005.09.004](https://doi.org/10.1016/j.compfluid.2005.09.004).

- [24] C. Zhang, R. Guy, B. Mulloney, Q. Zhang, T. Lewis, Neural mechanism of optimal limb coordination in crustacean swimming, *Proceedings of the National Academy of Sciences of the USA* 38 (2014) 13840–13845. doi:[10.1073/pnas.1323208111](https://doi.org/10.1073/pnas.1323208111).
- [25] R. P. Beyer, R. LeVeque, Analysis of a one-dimensional model for the immersed boundary method, *SIAM Journal on Numerical Analysis* 29 (1992) 332–364. doi:[10.1137/0729022](https://doi.org/10.1137/0729022).
- [26] D. Goldstein, R. Handler, L. Sirovich, Modeling a no-slip flow boundary with an external force field, *Journal of Computational Physics* 105 (1993) 354–366. doi:[10.1006/jcph.1993.1081](https://doi.org/10.1006/jcph.1993.1081).
- [27] M. Lai, C. S. Peskin, An immersed boundary method with formal second-order accuracy and reduced numerical viscosity, *Journal of Computational Physics* 160 (2000) 705–719. doi:[10.1006/jcph.2000.6483](https://doi.org/10.1006/jcph.2000.6483).
- [28] J. M. Teran, C. S. Peskin, Tether force constraints in Stokes flow by the immersed boundary method on a periodic domain, *SIAM Journal of Scientific Computing* 31 (5) (2009) 3404–3416. doi:[10.1137/080720217](https://doi.org/10.1137/080720217).
- [29] H. D. Ceniceros, J. E. Fisher, A. M. Roma, Efficient solutions to robust, semi-implicit discretizations of the immersed boundary method, *Journal of Computational Physics* 228 (2009) 7137–7158. doi:[10.1016/j.jcp.2009.05.031](https://doi.org/10.1016/j.jcp.2009.05.031).
- [30] R. D. Guy, B. Philip, B. E. Griffith, Geometric multigrid for an implicit-time immersed boundary method, *Advances in Computational Mathematics* 41 (2015) 635–662. doi:[10.1007/s10444-014-9380-1](https://doi.org/10.1007/s10444-014-9380-1).
- [31] D. B. Stein, R. D. Guy, B. Thomases, Immersed boundary smooth extension: A high-order method for solving pde on arbitrary smooth domains using Fourier spectral methods, *Journal of Computational Physics* 304 (2016) 252–274. doi:[10.1016/j.jcp.2015.10.023](https://doi.org/10.1016/j.jcp.2015.10.023).
- [32] B. E. Griffith, X. Luo, Hybrid finite difference/finite element immersed boundary method, *International Journal for Numerical Methods in Biomedical Engineering* 33 (12) (2017) e2888. doi:[10.1002/cnm.2888](https://doi.org/10.1002/cnm.2888).
- [33] V. Flamini, A. DeAnda, B. E. Griffith, Immersed boundary-finite element model of fluid-structure interaction in the aortic root, *Theoretical and Computational Fluid Dynamics* 30 (1) (2016) 139–164. doi:[10.1007/s00162-015-0374-5](https://doi.org/10.1007/s00162-015-0374-5).
- [34] C. Pozrikidis, *A Practical Guide to Boundary Element Methods*, Chapman & Hall, 2002.
- [35] A. Mayo, The fast solution of poisson’s and the biharmonic equations on irregular regions, *SIAM Journal on Numerical Analysis* 21 (2) (1984) 285–299. doi:[10.1137/0721021](https://doi.org/10.1137/0721021).

- [36] C. Carvalho, S. Khatri, A. D. Kim, Asymptotic approximations for the close evaluation of double-layer potentials, *SIAM Journal of Scientific Computation* 42 (1) (2020) A504–A533. doi:[10.1137/18M1218698](https://doi.org/10.1137/18M1218698).
- [37] H. Power, G. Miranda, Second kind integral equation formulation of Stokes’ flows past a particle of arbitrary shape, *SIAM Journal on Applied Mathematics* 47 (4) (1987) 689–698. doi:[10.1137/0147047](https://doi.org/10.1137/0147047).
- [38] M. Ingber, L. Mondy, Direct second kind boundary integral formulation for Stokes flow problems, *Computational Mechanics* 11 (1) (1993) 11–27. doi:[10.1007/BF00370070](https://doi.org/10.1007/BF00370070).
- [39] F. B. Usabiaga, B. Kallemov, B. Delmotte, A. Bhalla, B. Griffith, A. Donev, Hydrodynamics of suspensions of passive and active particles: A rigid multiblob approach, *Communications in Applied Mathematics and Computational Science* 11 (2) (2016) 217–296. doi:[10.2140/camcos.2016.11.217](https://doi.org/10.2140/camcos.2016.11.217).
- [40] J. D. Eldredge, A method of immersed layers on Cartesian grids, with application to incompressible flows, *Journal of Computational Physics* 448 (110716) (2022). doi:[10.1016/j.jcp.2021.110716](https://doi.org/10.1016/j.jcp.2021.110716).
- [41] M. Benzi, G. H. Golub, J. Liesen, Numerical solution of saddle point problems, *Acta Numerica* 14 (2005) 1–137. doi:[10.1017/S0962492904000212](https://doi.org/10.1017/S0962492904000212).
- [42] T. M. Inc., *Matlab version: 9.12.0 (R2022a)* (2022). URL <https://www.mathworks.com>
- [43] K. E. Atkinson, *The Numerical Solution of Integral Equations of the Second Kind*, Cambridge University Press, 1997.
- [44] D. Colton, R. Kress, *Integral Equation Methods in Scattering Theory*, John Wiley & Sons, 1983.
- [45] J. F. Ahner, Some spectral properties of an integral operator in potential theory, *Proceedings of the Edinburgh Mathematical Society* 29 (3) (1986) 405–411. doi:[10.1017/S0013091500017843](https://doi.org/10.1017/S0013091500017843).
- [46] J. T. Beale, M. Lai, A method for computing nearly singular integrals, *SIAM Journal of Numerical Analysis* 38 (6) (2001) 1902–1925. doi:[10.1137/S0036142999362845](https://doi.org/10.1137/S0036142999362845).
- [47] A. Klockner, A. Barnett, L. Greengard, M. O’Neil, Quadrature by expansion: A new method for the evaluation of layer potentials, *Journal of Computational Physics* 252 (2013) 332–349. doi:[10.1016/j.jcp.2013.06.027](https://doi.org/10.1016/j.jcp.2013.06.027).
- [48] W.-P. Breugem, A second-order accurate immersed boundary method for fully resolved simulations of particle-laden flows, *Journal of Computational Physics* 231 (13) (2012) 4469–4498. doi:<https://doi.org/10.1016/j.jcp.2012.02.026>.

- [49] Y. Mori, C. S. Peskin, Implicit second-order immersed boundary methods with boundary mass, *Computer Methods in Applied Mechanics and Engineering* 197 (25) (2008) 2049–2067. doi:<https://doi.org/10.1016/j.cma.2007.05.028>.
- [50] B. E. Griffith, R. D. Hornung, D. M. McQueen, C. S. Peskin, An adaptive, formally second order accurate version of the immersed boundary method, *Journal of Computational Physics* 223 (1) (2007) 10–49. doi:<https://doi.org/10.1016/j.jcp.2006.08.019>.
- [51] J. Saranen, G. Vainikko, *Periodic Integral and Pseudodifferential Equations with Numerical Approximation*, Springer, 2000.
- [52] H. Power, The completed double layer boundary integral equation method for two-dimensional stokes flow, *IMA Journal of Applied Mathematics* 51 (1993) 123–145. doi:[10.1093/imamat/51.2.123](https://doi.org/10.1093/imamat/51.2.123).
- [53] G. C. Hsiao, R. Kress, On an integral equation for the two-dimensional exterior stokes problem, *Applied Numerical Mathematics* 1 (1) (1985) 77–93. doi:[10.1016/0168-9274\(85\)90029-7](https://doi.org/10.1016/0168-9274(85)90029-7).
- [54] F.-K. Hebeker, Efficient boundary element methods for three-dimensional exterior viscous flows, *Numerical Methods for Partial Differential Equations* 2 (4) (1986) 273–297. doi:[10.1002/num.1690020404](https://doi.org/10.1002/num.1690020404).
- [55] A. Goza, S. Liska, B. Morley, T. Colonius, Accurate computation of surface stresses and forces with immersed boundary methods, *Journal of Computational Physics* 321 (2016) 860–783. doi:[10.1016/j.jcp.2016.06.014](https://doi.org/10.1016/j.jcp.2016.06.014).
- [56] C. Pozrikidis, *Boundary integral and singularity methods for linearized viscous flow*, Cambridge University Press, 1992.

This figure "FD_2dx_changedm.jpg" is available in "jpg" format from:

<http://arxiv.org/ps/2203.12126v3>

This figure "FD_fixm_changeds.jpg" is available in "jpg" format from:

<http://arxiv.org/ps/2203.12126v3>

This figure "FD_sin_Changing_ms.jpg" is available in "jpg" format from:

<http://arxiv.org/ps/2203.12126v3>

This figure "FD_spect_slice_coarse.jpg" is available in "jpg" format from:

<http://arxiv.org/ps/2203.12126v3>

This figure "FD_spectral_slice_fine.jpg" is available in "jpg" format from:

<http://arxiv.org/ps/2203.12126v3>

This figure "FD_x_Changing_ms.jpg" is available in "jpg" format from:

<http://arxiv.org/ps/2203.12126v3>

This figure "IBDLQplot_ds1.jpg" is available in "jpg" format from:

<http://arxiv.org/ps/2203.12126v3>

This figure "IBDLQplot_ds2.jpg" is available in "jpg" format from:

<http://arxiv.org/ps/2203.12126v3>

This figure "IBDL_Poisson_refinement.jpg" is available in "jpg" format from:

<http://arxiv.org/ps/2203.12126v3>

This figure "IBDL_Q_convergence_ds1.jpg" is available in "jpg" format from:

<http://arxiv.org/ps/2203.12126v3>

This figure "IBDL_Q_convergence_ds2.jpg" is available in "jpg" format from:

<http://arxiv.org/ps/2203.12126v3>

This figure "IBDLinterioreerrorplot.jpg" is available in "jpg" format from:

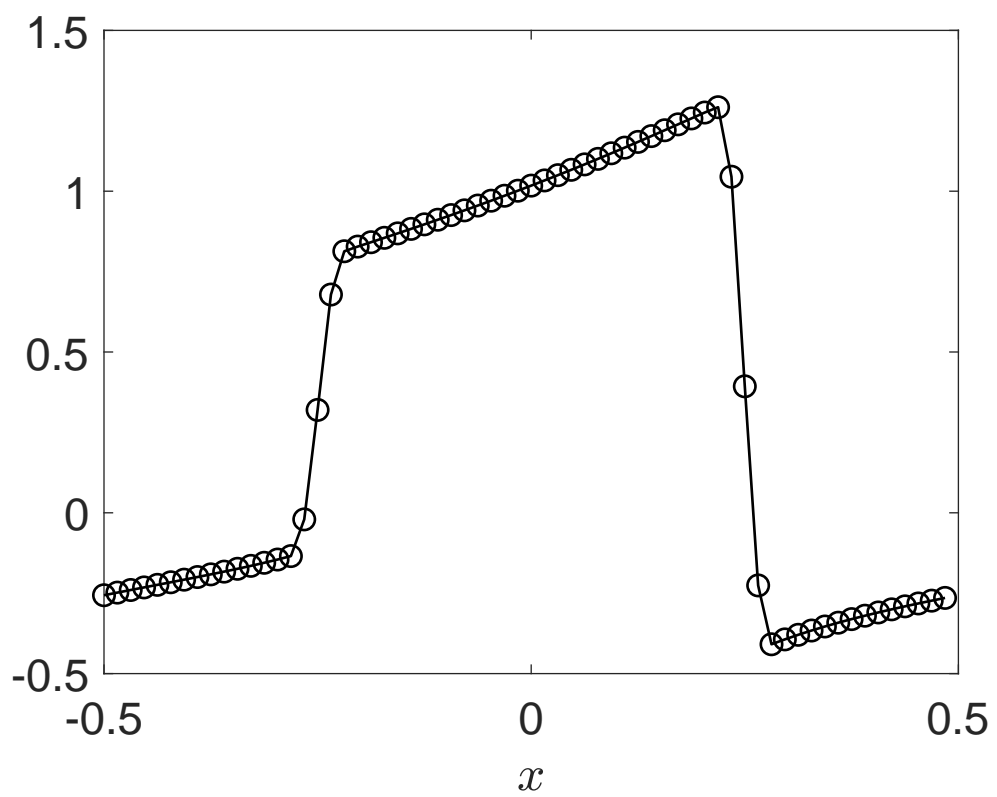
<http://arxiv.org/ps/2203.12126v3>

This figure "IBDLinteriorrefinement.jpg" is available in "jpg" format from:

<http://arxiv.org/ps/2203.12126v3>

This figure "IBDLsolutionplot.jpg" is available in "jpg" format from:

<http://arxiv.org/ps/2203.12126v3>



This figure "IBDLsolutionslice.jpg" is available in "jpg" format from:

<http://arxiv.org/ps/2203.12126v3>

This figure "IBSLFplot_ds1.jpg" is available in "jpg" format from:

<http://arxiv.org/ps/2203.12126v3>

This figure "IBSL_F_convergence_ds1.jpg" is available in "jpg" format from:

<http://arxiv.org/ps/2203.12126v3>

This figure "Spectral_sin_Changing_ms1.jpg" is available in "jpg" format from:

<http://arxiv.org/ps/2203.12126v3>

This figure "Spectral_x_Changing_ms1.jpg" is available in "jpg" format from:

<http://arxiv.org/ps/2203.12126v3>

This figure "IBSLFplot_ds2.jpg" is available in "jpg" format from:

<http://arxiv.org/ps/2203.12126v3>

This figure "IBSL_F_convergence_ds2.jpg" is available in "jpg" format from:

<http://arxiv.org/ps/2203.12126v3>

This figure "IBSLinteriorerrorplot.jpg" is available in "jpg" format from:

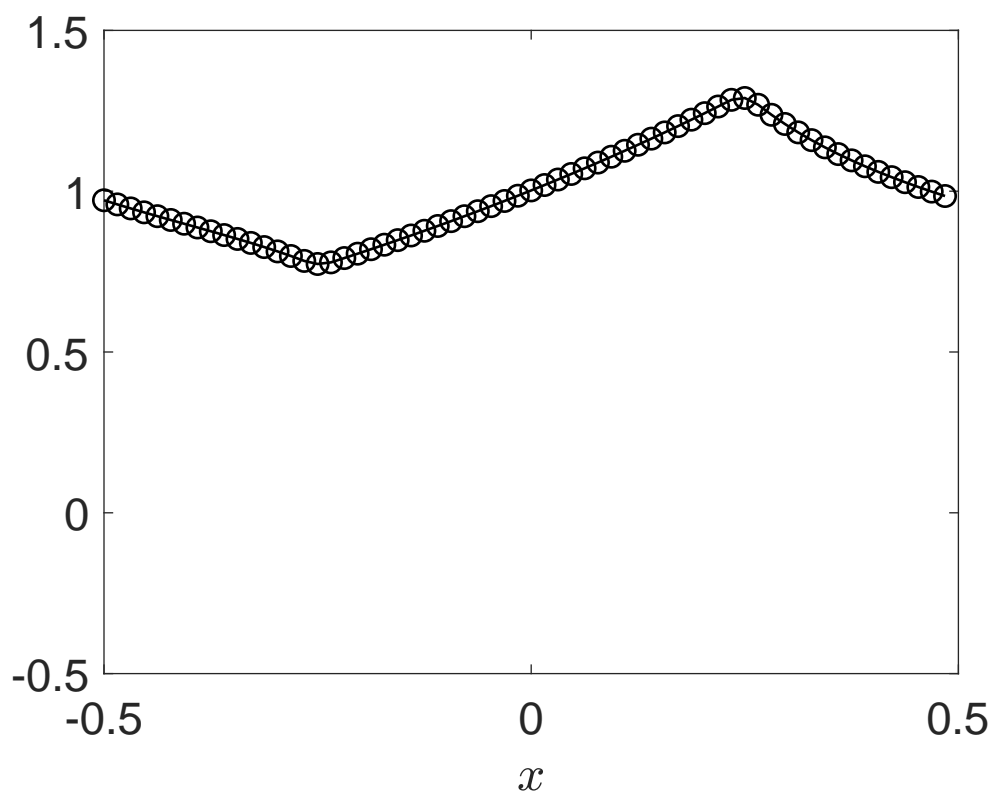
<http://arxiv.org/ps/2203.12126v3>

This figure "IBSLinteriorrefinement.jpg" is available in "jpg" format from:

<http://arxiv.org/ps/2203.12126v3>

This figure "IBSLsolutionplot.jpg" is available in "jpg" format from:

<http://arxiv.org/ps/2203.12126v3>



This figure "IBSLsolutionslice.jpg" is available in "jpg" format from:

<http://arxiv.org/ps/2203.12126v3>

This figure "Spectral_sin_Changing_ms2.jpg" is available in "jpg" format from:

<http://arxiv.org/ps/2203.12126v3>

This figure "Spectral_x_Changing_ms2.jpg" is available in "jpg" format from:

<http://arxiv.org/ps/2203.12126v3>

This figure "Neumann_Ub_no_filter_075.jpg" is available in "jpg" format from:

<http://arxiv.org/ps/2203.12126v3>

This figure "Neumann_no_filter_075.jpg" is available in "jpg" format from:

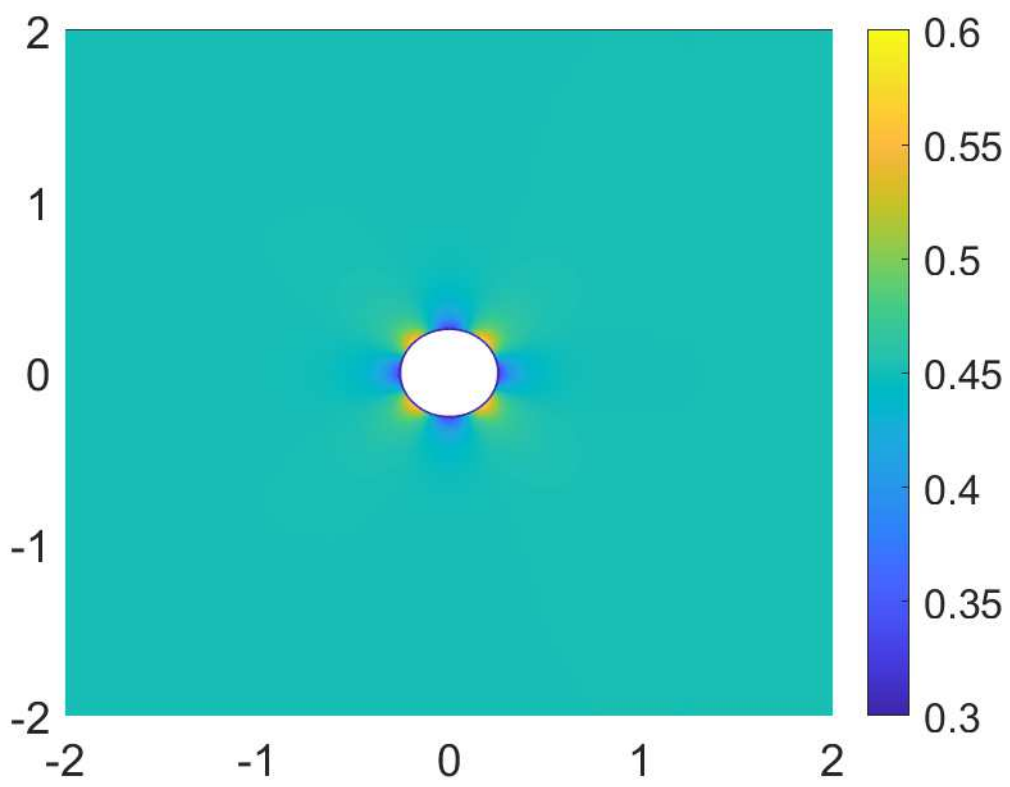
<http://arxiv.org/ps/2203.12126v3>

This figure "bigLexp.jpg" is available in "jpg" format from:

<http://arxiv.org/ps/2203.12126v3>

This figure "bigLexpcompleted.jpg" is available in "jpg" format from:

<http://arxiv.org/ps/2203.12126v3>



This figure "bigLexperror.jpg" is available in "jpg" format from:

<http://arxiv.org/ps/2203.12126v3>

This figure "condplot.jpg" is available in "jpg" format from:

<http://arxiv.org/ps/2203.12126v3>

This figure "courseerrorplot.jpg" is available in "jpg" format from:

<http://arxiv.org/ps/2203.12126v3>

This figure "exteriordomain.jpg" is available in "jpg" format from:

<http://arxiv.org/ps/2203.12126v3>

This figure "exteriordomainsolution.jpg" is available in "jpg" format from:

<http://arxiv.org/ps/2203.12126v3>

This figure "fineerrorplot.jpg" is available in "jpg" format from:

<http://arxiv.org/ps/2203.12126v3>

This figure "interiordomain.jpg" is available in "jpg" format from:

<http://arxiv.org/ps/2203.12126v3>

This figure "interpolationimage.jpg" is available in "jpg" format from:

<http://arxiv.org/ps/2203.12126v3>

This figure "iterationcountsplot.jpg" is available in "jpg" format from:

<http://arxiv.org/ps/2203.12126v3>

This figure "nointerperrorplot.jpg" is available in "jpg" format from:

<http://arxiv.org/ps/2203.12126v3>

This figure "nointerfigures.jpg" is available in "jpg" format from:

<http://arxiv.org/ps/2203.12126v3>

This figure "slicestogether.jpg" is available in "jpg" format from:

<http://arxiv.org/ps/2203.12126v3>

This figure "smallLexp.jpg" is available in "jpg" format from:

<http://arxiv.org/ps/2203.12126v3>